

AD-A172 478

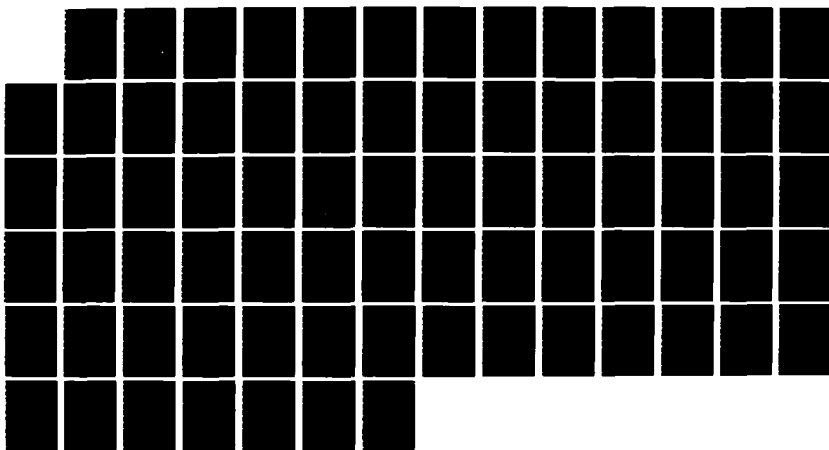
STUDIES OF GAS TURBINE HEAT TRANSFER: AIRFOIL SURFACE
AND END-WALL (U) MINNESOTA UNIV MINNEAPOLIS HEAT
TRANSFER LAB E R ECKERT ET AL APR 86 AFOSR-TR-86-0854
F49620-85-C-0049

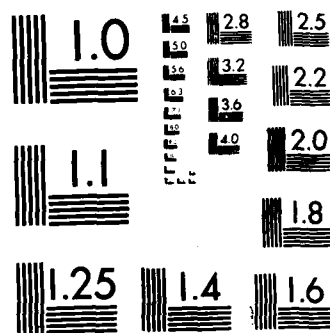
1/1

UNCLASSIFIED

F/G 21/5

NL





MICROCOPY RESOLUTION TEST CHART
NATIONAL BUREAU OF STANDARDS-1963-A

UNCLASSIFIED

SECURITY CLASSIFICATION OF THIS PAGE (When Data Entered)

REPORT DOCUMENTATION PAGE		READ INSTRUCTIONS BEFORE COMPLETING FORM
1. REPORT NUMBER AFOSR-TR- 86-0854	2. GOVT ACCESSION NO.	3. RECIPIENT'S CATALOG NUMBER
4. TITLE (and Subtitle) STUDIES OF GAS TURBINE HEAT TRANSFER: AIRFOIL SURFACE AND END-WALL		5. TYPE OF REPORT & PERIOD COVERED Annual Progress Report 1/3/85 - 2/28/86
7. AUTHOR(s) E. R. G. Eckert, R. J. Goldstein and T. W. Simon		6. PERFORMING ORG. REPORT NUMBER
9. PERFORMING ORGANIZATION NAME AND ADDRESS Heat Transfer Laboratory, Mechanical Engineering Department, University of Minnesota, Minneapolis, Minnesota 55455		8. CONTRACT OR GRANT NUMBER(s) F49620-85-C-0049
11. CONTROLLING OFFICE NAME AND ADDRESS AFOSR, Bolling Air Force Base Washington, D.C. 20332		10. PROGRAM ELEMENT, PROJECT, TASK AREA & WORK UNIT NUMBERS 6112F-2307/A1
14. MONITORING AGENCY NAME & ADDRESS (if different from Controlling Office) Same as 11		12. REPORT DATE 1 March 1985-28 February 1986
		13. NUMBER OF PAGES 154
		15. SECURITY CLASS. (of this report) Unclassified
		15a. DECLASSIFICATION/DOWNGRADING SCHEDULE
16. DISTRIBUTION STATEMENT (of this Report) Approved for public release; distribution unlimited.		
17. DISTRIBUTION STATEMENT (of the abstract entered in Block 20, if different from Report) Approved for public release; distribution unlimited.		
18. SUPPLEMENTARY NOTES		
19. KEY WORDS (Continue on reverse side if necessary and identify by block number) Gas Turbines, Heat Transfer, Cascades, End-Wall		
20. ABSTRACT (Continue on reverse side if necessary and identify by block number) The annual report documents progress at the University of Minnesota Heat Transfer Laboratory on the topic of heat transfer from gas turbine airfoil and end-wall surfaces. Subtopics are: Curvature effects, End-wall heat transfer and Near-end-wall heat transfer. Curvature effects on turbulent transport are shown for a smooth convex wall and for single-row film-cooled convex and concave walls. End-wall mass (heat) transfer coefficient contours show the horseshoe vortex, the passage vortex and an inner vortex.		

AD-A172 470

DTIC FILE COPY

DTIC
ELECTE
S OCT 02 1986 **D**
E

DD FORM 1473

JAN 73

EDITION OF 1 NOV 65 IS OBSOLETE
S/N 0102-LF-014-6601

UNCLASSIFIED

SECURITY CLASSIFICATION OF THIS PAGE (When Data Entered)

165400 PM

86-10-01-141

AFOSR-TR. 86-0854

Approved for public release;
distribution unlimited.

Annual Progress Report
(1 March 1985 - 28 February 1986)

STUDIES OF GAS TURBINE HEAT TRANSFER
AIRFOIL SURFACE AND END-WALL

AFOSR GRANT # F49620-85-C-0049
(1 March 1983 - 30 April 1987)

E. R. G. Eckert, R. J. Goldstein, T. W. Simon
Co-Principal Investigators

April 1986

AIR FORCE OFFICE OF SCIENTIFIC RESEARCH (AFSC)
NOTICE OF TRANSMITTAL TO DTIC
This technical report has been reviewed and is
approved for public release IAW AFR 190-12.
Distribution is unlimited.
MATTHEW J. KETTER
Chief, Technical Information Division



Accession For	
NTIS GRA&I	<input checked="checked" type="checkbox"/>
DTIC TAB	<input type="checkbox"/>
Unannounced	<input type="checkbox"/>
Justification	
By _____	
Distribution/ _____	
Availability Codes	
Dist	Avail and/or Special
A-1	

INTRODUCTION

The following annual progress report documents work at the University of Minnesota Heat Transfer Laboratory, under AFOSR sponsorship, on the topic of heat transfer from gas turbine airfoil and end-wall surfaces. The research was divided into the following three subtopics: Curvature Effects and End-Wall and Near-End-Wall Heat Transfer. Progress on each is discussed separately.

A. The Effect of Convex Curvature on Heat Transfer and Hydrodynamics of Turbulent Boundary Layers

Three experiments were conducted to investigate the effect of streamwise curvature over the range from $\delta/R = 0.01$ to 0.04 and to study the effect of free-stream turbulence on fully turbulent curved boundary layers. An attached fully turbulent boundary layer, grown on a flat plate is introduced to a convex wall of constant radius of curvature followed by a flat recovery wall (Figure 1). Descriptors of the three experiments are listed in Table 1.

1. Objectives

The effects of varying the radius of curvature on curved, two-dimensional boundary layers, including the recovery process, were investigated to further understand the transport mechanism and to extend the data base for prediction model development. Two different free-stream turbulence intensity cases were employed to study the effects of free-stream turbulence intensity on the curved boundary layer. The higher turbulence intensity case, Case 3, showed indications of interactions between the outer

(unheated) and the inner (heated) shear layers for $x > 150$ cm in the recovery station. Significant additions to the previous data base are:

- (1) The recovery process, with heat transfer, was investigated for cases of milder curvature than that of the previous studies.
- (2) The radius of curvature was varied from case to case in the same study.
- (3) Curvature effects of δ/R between those of mild and strong curvature were investigated in the same facility.
- (4) Free-stream turbulence intensity effects on the curved boundary layer were investigated for the first time.

2. Progress and Accomplishments

The important observations from the three cases of experiments are summarized based on You (1986); You, Simon and Kim (1986a) and You, Simon and Kim (1986b)--the second and third references are attached:

(A) General characteristics of convex-curved boundary layers: CASE 1

- (1) Profiles of mean velocity and temperature show shortened log-linear regions and enhanced wake regions in the curve. The recovery of these mean profiles in the log-linear region is complete by about 80 cm of recovery length. The wake is decreasing slightly near the end of the recovery, indicating incomplete recovery.
- (2) The curvature effect increases the turbulent Prandtl number in the log-linear region by about 25% for Case 1.
- (3) Reduced rates of growth of momentum thickness and increased shape factor within the curve due to the effect of a decrease in the turbulent transport are observed. The recovery of the shape factor H is not complete at the end of the recovery section.
- (4) Rapid decreases of St and $C_f/2$ at the beginning of the curve are observed, followed by slow decreases within the curve (Figure 2). Decreases from expected flat-wall values are 20% for Case 1 ($\delta/R = 0.03$). The recovery process is extremely slow with St recovery leading $C_f/2$ --an increase of $2St/C_f$.
- (5) Streamwise-normal turbulence intensity profiles (Figure 3) show a fast response to the introduction of curvature with a drastic reduction of the near-wall peak. The self-similar shape is attained by station 4 and continues through the

remainder of the curve. The recovery process begins with an increase of turbulence intensity near the wall at $y/\delta = 0.1-0.2$ propagating slowly to the outer layers. Shear stress profiles respond quickly to curvature, reducing to about 55% of the upstream flat-plate values for $\delta/R = 0.03$. Recovery occurs slowly, with the wake recovering faster than the near-wall flow.

(B) Effect of radius of curvature: Comparison between CASE 1 and CASE 2

- (1) Though both Cases 1 and 2 show the same trends, the effects of the different strengths of curvature are clearly observable.
- (2) Decreased St and $C_f/2$ of about 10% from expected flat-wall values are observed for Case 2 ($\delta/R = 0.013$) whereas decreases of about 20% are observed for Case 1 ($\delta/R = 0.03$) --Figure 2. The ratio of boundary layer thickness to the radius of curvature is the appropriate scaling parameter over the range from $\delta/R = 0.01$ to $\delta/R = 0.04$.
- (3) The turbulent Prandtl number in the log-linear region shows a 20% increase for Case 2.
- (4) "Asymptotic" behavior, suggested by Gillis and Johnston (1983) is observed.
- (5) Shear stress profiles, plotted in $-u'v'/U_{pw}^2$ vs. y/δ , show the realization of a self-similar shape by station 3 even in the weaker curvature case.

(C) Effect of free-stream turbulence intensity: Comparison between CASE 1 and CASE 3

- (1) The curvature effect dominates the free-stream turbulence effect for the cases studied ($\delta/R = 0.03$).
- (2) In Figure 4, flat-plate data at $x = -29.9$ cm show reduced wake strength and about 5% increases in St and $C_f/2$ due to the higher free-stream turbulence intensity (1.85%).
- (3) Higher free-stream turbulence intensity causes a stronger curvature effect on hydrodynamic transport than on thermal transport (Figure 4): $C_f/2$ within the convex-curved section decreases more than St decreases, which is consistent with the decrease of log-linear region Pr_t near the end of the curved section.
- (4) Profiles of turbulence measurements show the same trends for the three cases: dramatic response to the entry of

curvature, asymptotic turbulent shear stress profiles and slow recovery.

- (5) Similar streamwise turbulence intensity profiles for Cases 1 and 3 near the end of the curve were found in spite of the different streamwise turbulence intensity profiles at station 1 (the difference in profiles was a result of the different free-stream turbulence intensities).
- (6) Reynolds shear stress profiles are dramatically influenced by curvature--the Reynolds shear stress data of $y/\delta > 0.7$ becomes negative at station 4. A self-similar shear stress profile in $-u'v'/U_{pw}^2$ vs. y/δ coordinates in the curved section was realized inside 50% of the shear layer thickness.

(D) The curvature effect on the wake

- (1) Coles wake law is valid in the convex-curved boundary layer when an appropriate wake parameter is found, using:

$$\Pi = (\kappa/2) \left[\frac{U_{pw}}{U_\tau} \frac{1}{1+\delta/R} - \left\{ (1/\kappa) \ln(\delta U_\tau / \nu) + C \right\} \right]$$

- (2) The variation of the wake parameter in the curved flow is different than that observed for flat-plate equilibrium cases (Figure 5); but, the variation is consistent for the two low-turbulence cases.
- (3) The effect of curvature on the wake parameter shows consistent trends with the other measurements: a stronger effect for stronger curvature and an extremely slow recovery.
- (4) The distribution of the wake components in the higher turbulence case (Case 3) did not indicate similarity with Coles wake law.

3. Expected Activities

The convex boundary layer study has been completed.

B. Modeling of Curved Turbulent and Transitional Flows

1. Objectives

- (1) Test transition models against recent data.

(2) Test curvature corrections to turbulent models against recent data.

(3) Improve transition and turbulent models.

2. Progress and Accomplishments

(1) Test of an all-laminar boundary layer flow.

An all-laminar flow was simulated using STAN5 (Crawford and Kays, 1976), a computer code for solving two-dimensional boundary layer flows. The data was of the qualification test for the transitional boundary layer experiment of Wang, Simon and Buddhavarapu (1985). Measurements were taken in an all-laminar flow over a flat plate with a constant heat flux. The predictions showed the effect streamwise acceleration on the skin friction coefficient and Stanton number.

(2) Modifications to STAN5.

STAN5 was modified mainly to employ the transition models and curvature modifications to the MLH turbulence model. In the main program, four transition start models and three transition length models were added. Three transition path models and two curvature models were employed in one subroutine. The input programming was modified so that the models can be selected and so that the turbulent Prandtl number could be input as a function of streamwise distance.

In addition, the property subroutine was revised so that SI units can be used, and the calculation and printout of Reynolds shear stress and turbulent heat flux was added.

(3) Test of transition model.

(i) Transition start model (Figure 6 a, b)

Transition models were tested against recent data taken by Wang, Simon and Buddhavarapu (1985) for freestream turbulence intensity of 0.68% and

2.0% over a flat plate with a constant heat flux. In both cases, the Abu-Ghannam and Shaw (1980) model predicts the transition start very well. Seyb (1972), Dunham (1972) and van Driest and Blumer (1963) models predicted a late start. Abu-Ghannam and Shaw was therefore selected as the transition start model.

(ii) Transition length model (Figure 7 a, b)

With the Abu-Ghannam and Shaw (1980) start model and the Dhawan and Narasimha (1958) path model, three transition length models were tested. The results showed that the Chen and Thyson (1971) and Debruge (1970) models predict short transition lengths resulting in a steeper increase in Stanton number in the transition region. The Dhawan and Narasimha model yields a steeper response than the experimental data would indicate but is superior to the other two.

(iii) Transition path model (Figure 8 a, b)

Among the three path (intermittency) models; Dhawan and Narasimha (1958), Abu-Ghannam and Shaw (1980), and Chen and Thyson (1971), the Dhawan and Narasimha model gives a better comparison to the data than do the others.

(4) Test of curvature model. (Figure 9 a, b, c)

The Adams and Johnston (1983) and the Bradshaw (1973) curvature modifications to the MLH turbulence model were tested against recent turbulent data over a convex-curved wall measured by You (1986) and You, Simon and Kim (1986a, 1986b). In the three cases tested, the Adams and Johnston model shows good agreement with the experimental data.

(5) Test of the combined model against curved-wall transition data

The combined model with the three transition models, Abu-Ghannam and Shaw (start), Dhawan and Narasimha (length), Dhawan and Narasimha (path),

and Adams and Johnston (turbulent curvature model) was tested against the convex-curved wall transition data (Wang and Simon, 1985). In the higher turbulence intensity (2%) case, the combined models' results compared well as can be seen in Figures 10 and 11.

Through the tests of the transition and curvature models using the mixing length hypothesis turbulence model, it was found that:

- (i) the start of transition is predicted well by the Abu-Ghannam and Shaw model (1980).
- (ii) the Dhawan and Narasimha (1958) models predict the transition length and path better than the other models tested.
- (iii) the predicted onset of transition is late and the transition path is rather rapid compared to the data.
- (iv) the combined model of the transition and turbulence curvature models is applicable and accurately calculates the curved wall transition data.

3. Expected Activities

The following will be continued:

- (1) Test of the selected models against other data sets
- (2) Improvement of the models
- (3) A study of the low Reynolds number version K- ϵ model

C. Measurement of the Turbulent Transport of Heat

1. Objectives

The objective for this portion of the work was to develop a probe which could be used to measure the turbulent transport of heat, $v't'$.

2. Progress and Accomplishments

The probe design, fabrication and qualification is now complete. The following summarizes.

Design of Probe. In designing special purpose hot-wire arrays, consideration must be given to a multitude of factors, some of which are spatial averaging, prong and shaft interference, end conduction, sensor cross-talk, and survivability. Ideally, one would like a probe whose active length was smaller than the smallest scales of interest while maintaining practicality of assembly and sensor strength. Since the Kolmogorov scale of laboratory turbulence typically ranges from 5 μm to 100 μm , sensors of this type are, as of yet, impossible to build. Compromises must therefore be made.

The choice of wire length and diameter was guided by the four criteria presented by Blair and Bennett (1984): (1) Reduction of mean flow gradients. The gradients of velocity and temperature along the wire were reduced by choosing the smallest wire length possible subject to other considerations. The ratio between boundary layer thickness and wire height was a minimum of 60 at all times. (2) Reduction of end effects. End effects were reduced by choosing a length to diameter (l/d) of 200, as recommended by Champagne (1967). This also enabled the correction equations recommended by Champagne (1967) to be employed. The active length consisted of only the central one-third of the wire, the ends of the wire being plated to reduce end losses further. (3) Practicality of fabrication and sensor survivability. The smallest wires commonly used for hot wire sensors are of 2.5 μm plated tungsten. These wires combine the strength of tungsten with the non-reactive nature of platinum. The wires can therefore be operated at high temperatures with good survivability. Furthermore, platinum presents a smooth surface to the flow, minimizing calibration drift due to accumulation of dust on the wire. (4) Assurance of adequate spacial resolution. The spatial resolution of the wire may be calculated from the curves presented

by Wyngaard (1968). It is found that for turbulence scales greater than 10 Kolmogorov scales, signal attenuation is negligible.

The distance between the prongs is determined by the practicality of fabrication, interference effects, and spatial resolution. The transverse correlation coefficient falls rapidly with sensor separation, as pointed out by Sandborn (1972) and Fulachier (1978). The sensors should therefore be placed as close as possible, but not so close as to interfere with one another. A transverse spacing between the X-array of 0.78 mm was chosen.

The configuration of the wires is as shown on Figure 12. The probe consists of three wires located in three parallel planes. The two outer wires are orthogonal, forming an X-array, while the third center wire is parallel to one of the outer wires. The two outer wires are operated at the same overheat ($OH=1.9$), while the center wire is operated at a much lower overheat ($OH=1.035$). The instantaneous temperature is then found from the two parallel wires, and the instantaneous velocity from the two outer wires, as will be shown in the data reduction section.

Response Equations. The mean response equation of each sensor is assumed to be of the form

$$Nu = A_1 + B_1 Re^{0.35} \quad (1)$$

which is a slight variation of King's law. This equation may be rewritten

$$U_{\infty}^{0.435} = AT_{\infty}^{0.76} + \frac{B}{(T_w - T_{\infty})} v_{ane}^2 \quad (2)$$

where A and B are assumed constant. This is the equation used by Blair and Bennett (1984) in modelling sensor response. The author has found, however, that A and B are slight functions of temperature. This variation is

incorporated into the response equation using a least-squares fit to the data. The final response equation is given by

$$U_{\infty}^{0.435} = (m_A T_{\infty} + b_A) T_{\infty}^{0.76} + \frac{(m_B T_{\infty} + b_B)}{(T_w - T_{\infty})} V_{ane}^2 \quad (3)$$

For isothermal flows, i.e., $T_{\infty} = \text{constant}$, the response equation reduces to

$$U_{\infty}^{0.435} = A + B V_{ane}^2 \quad (4)$$

Data Reduction. The two assumptions made when reducing the data are (1) the boundary layer is two-dimensional and (2) the instantaneous velocities seen by the two parallel wires are equal. The first assumption is needed since the third component of velocity (w) cannot be determined. If the probe is aligned with the flow, however, and if the boundary layer is two-dimensional, the w -component makes only second order contributions to sensor response and may be safely neglected. If the second assumption holds, the velocity term (U_{eff}) may be eliminated from the response equations for the two parallel wires, resulting in an equation solely in terms of the ambient temperature, T_{∞} . The ambient temperature may be found by iteratively solving for T_{∞} using the Newton-Raphson method.

The instantaneous velocities U and V may then be found from the two outer orthogonal wires using the k^2 relation given by Champagne (1967). Knowing the instantaneous values of U , V , and T , the rms fluctuation quantities (u' , v' , and t') and the cross correlations ($u'v'$, $u't'$, and $v't'$) may be determined. The equations used are given by

$$q'_1 = \sqrt{q'^2_1} = \sqrt{\frac{\sum q_1^2}{N-1} - \frac{(\sum q_1)^2}{N(N-1)}} \quad (5)$$

$$q'_1 q'_2 = \frac{\sum q_1 q_2}{N-1} - \frac{\sum q_1 \sum q_2}{N(N-1)} \quad (6)$$

where $q_i = u, v, \text{ or } t$, and $N = \text{number of samples}$.

Calibration Facility. A schematic of the calibration facility is shown on Figure 13. The calibration tunnel was designed and built by Wilson (1970). Temperature control was added as part of this project. A brief description follows.

Compressed air at a line pressure of 120 psi passes through a series of cleaning and regulating equipment before reaching the air heater. The heater is a coil taken from a household hair dryer inserted into a plexiglass tube. A 115 VAC wall outlet regulated by a voltage regulator (Variac) powers the coil. Overheating is prevented by a thermal switch which opens the circuit if the temperature becomes excessive. The heated air then passes into an insulated 10 gallon mixing tank. Since the temperature of the flow varies with the flow rate through the coil, and since an isothermal flow is needed, the total flow rate through the system must be kept constant. This may be achieved by keeping the pressure in the tank constant. The vent and control valves shown on the schematic perform this function. The control valve regulates the flow to the calibration tunnel, while the vent valve is adjusted until the pressure, as measured by a manometer, returns to a preset value. A relief valve prevents excessive pressure buildup in the tank.

The calibration tunnel consists of a stilling chamber with turbulence reducing screens and a honeycomb flow straightener, and an elliptical contraction followed by a calibration chamber and a nozzle. The flow exiting the nozzle was found to have a turbulence intensity of 0.3%. The flow could be continuously varied from 0 m/s to as high as 130 m/s with the appropriate choice of exit nozzle. The temperature was found to be very uniform ($.01^{\circ}\text{C}$), and could be varied from room temperature ($\sim 25^{\circ}\text{C}$) to over 40°C .

Other Instrumentation.

Pressure Transducer: The transducer used is of the variable reluctance type (Validyne DP45), and is designed for low-range, differential measurements of extremely low pressure differences. The diaphragm used has a pressure range of 8.9 cm (3.5 in. H₂O) with an accuracy of 0.5% full scale. The response was found to be very linear throughout the entire operating range. Calibration of the transducer was performed against a micro-manometer (Dwyer Microtector) with an accuracy of ± 0.06 mm H₂O. The calibration curve was obtained by a linear fit to the data.

Carrier Demodulator: The analog output of the pressure transducer is sent to a demodulator (Validyne CD-15) which provides a stable DC output. The gain and offset on the demodulator enabled tailoring of the signal to maximize digitizing resolution.

A/D Converter: Three A/D converters were used--an HP 3437A system voltmeter and two Norland Prowler digital oscilloscopes. The former is a $3\frac{1}{2}$ digit successive approximation digitizer capable of sampling up to 3600 samples per second (ASCII mode). The latter is a 12 bit digitizer capable of simultaneously sampling two channels of data at speeds up to 100 kHz. Two buffers store up to 4096 data points each. Two Prowlers may also be hooked together as master and slave, enabling four channels of data to be taken simultaneously. Simple processing of the data can be done within the Norland using the built-in math, calculus, and signal processing routines, or the data may be sent via the IEEE-488 interface bus to the computer.

Computer: A Hewlett Packard Series 200 Model 16 personal computer with 512 K memory was used for data reduction and as a controller. The computer is linked with a dual disk drive (HP 9121) which utilizes 3.5 in., 256 K, single-sided micro diskettes, and with an inkjet printer (HP

Thinkjet). High level HP Basic is the programming language used. A co-processor (Infotek FP210) and a Basic Compiler (Infotek BC203) were added to speed data reduction. A 5-10 times increase in speed was realized. An IEEE-488 interface bus allowed communication with other instruments.

Anemometer: A four-channel constant-temperature anemometer (TSI IFA-100) was used to drive the hot-wires. The anemometer features a built-in microprocessor with non-volatile memory which monitors and stores set-up parameters for future use. The high frequency response and high signal-to-noise ratio gives accurate measurements even in low turbulence intensity flows. A built-in square wave generator enables the frequency response to be determined. Also, the built-in signal conditioners are used to tailor the output signal, maximizing the digitizing resolution of the A/D converters.

Calibration of the Probe. The probe must be calibrated as a function of both velocity and temperature. It was decided to calibrate the probe for velocity at one temperature, then change temperatures, thus obtaining a calibration curve of anemometer voltage vs. velocity for each temperature setting.

A schematic of the set-up used is shown on Figure 14. The probe is driven by three of the four bridges on the anemometer. The signal conditioners offset and amplify the voltages, maximizing digitizing resolution. Two Norland Prowlers, wired as master and slave, simultaneously sample and digitize the anemometer signals. Two thousand data points over eight seconds are typically taken. The math processing capability of the Prowlers is used to internally average the signals, after which the averaged values are sent to the computer via the IEEE-488 data link. In the meantime, the HP 3437A A/D converter is used to sample the pressure

transducer signal. The data is sent to the computer for averaging. Three thousand points taken over 8 seconds is typical. The pressure transducer signal is used to find the velocity at the exit of the calibration jet through a calibration equation relating the transducer signal to the pressure drop at the jet exit. The jet temperature is measured with a thermocouple. The Fluke 8840A voltmeter samples the thermocouple voltage and sends the data to the computer on request. Twenty data points were taken per calibration curve, with more data points taken at lower velocities where the calibration curve is steep. The two outer wires were calibrated at an overheat of 1.9, while the center wire was calibrated at an overheat of 1.035.

The above setup enables calibration curves to be found quickly and accurately. The process is highly automated; the computer controls all data acquisition, with the experimenter having only to change the jet velocity and temperature.

In determining the calibration coefficients, the response equation given by equation (2) was assumed for each jet temperature. The velocity u_{∞} is not the jet velocity, but the effective cooling velocity given by Wilson (1970)

$$U_{eff} = U[(1 + k^2)^{0.5} \sin \theta] \quad (7)$$

where θ is the angle between the wire and the main flow direction. The factor k is introduced to account for cooling due to the velocity tangential to the sensor as discussed earlier. The wires used in this probe had $l/d = 200$. The coefficients A and B in equation (2) are obtained using a least squares fit to the data for two jet temperatures, typically 25°C and 30°C. The variation in A and B is then modelled using a linear fit and introduced into equation (2) to get the final response equation given by equation (3).

Qualification of the Probe. Qualification of the probe took place in a flat-plate turbulent boundary layer with a momentum thickness Reynolds number of $Re_\theta = 2670$ and a uniform wall heat flux boundary condition ($q'' = 226 \text{ W/m}^2$). The probe was traversed across the boundary layer and measurements of $u'v'$, t' , $u't'$, and $v't'$ were made. These quantities, normalized on the free-stream velocity (U_∞) and the wall to free-stream temperature difference ($T_w - T_\infty$), were compared with the boundary layer data of Blair and Bennett (1984) and Gibson and Verriopoulos (1984). All profiles agreed within the uncertainty of the measurement (estimated to be 15%). As a further check on the validity of the data, profiles of apparant t' (the t' measured by the probe in an isothermal boundary layer) were measured. Apparant t' arises due to the two parallel wires not seeing the same velocity. Apparant t' values on the order of the actual t' values would indicate a problem with the probe. The results are shown on Figure 15. It may be seen that the apparant t' values are 5% to 10% of the actual t' values except very near the wall. The influence on the actual data is even smaller since the apparent t' affects the actual data in a root-sum-square manner. Interestingly enough, turbulence intensity is seen to have little effect on apparant t' . This suggests that distance from the wall rather than turbulence intensity is the controlling parameter.

Results and Discussion. Measurements were made in the flow discussed in section A of this report. The station locations are shown on Figure 1.

Low TI Case (TI=0.65%): Shear stress profiles are shown on Figure 16. The profiles are seen to respond quickly to curvature. A dramatic reduction at the onset of curvature is observed, after which the profiles slowly evolve to what appears to be an asymptotic state by station

6. Curvature is seen to reduce the shear stress by about 45% below the flat wall values throughout the curve. Recovery of shear stress is slow, with recovery seemingly complete in the wake by station 10. You, et al. (1986) have shown that the near wall values of $u'v'$ recover very slowly. All the trends are consistent with the observations of Gillis and Johnston (1983) and You, et al. (1986).

Profiles of t' are plotted on Figure 17. The flat upstream values (station 1) are seen to agree with the measurements of Blair and Bennett (1984) and Gibson and Verriopoulos (1984) within the uncertainty of the measurement. The profiles within the curve assume an asymptotic shape for $y/\delta < 0.5$. No evolution of the profiles, as was observed for the shear stress, is evident. Recovery has a dramatic effect on t' . Profiles of t' are seen to overshoot the station 1 profiles. It is believed that the profile shape eventually returns to that of station 1. The recovery length was too short to observe this in the present experiment, however.

The effects of curvature and recovery on the streamwise turbulent heat flux $u't'$ are shown on Figure 18. The station 1 values agree very well with the data of Gibson and Verriopoulos (1984). The effect of curvature on $u't'$ is dramatic. The profiles in the curve "snap" into an asymptotic shape for $y/\delta < 0.5$. Slow evolution of the profiles for $y/\delta > .05$ may be observed. Recovery is seen to cause an overshoot of $u't'$ beyond the station 1 values, although the profile is expected to return to the station 1 values given a long enough recovery length.

Profiles of the apparent turbulent heat flux $v't'$ are shown on Figure 19. The effects of curvature and recovery on $v't'$ are very similar to those observed for $u't'$ --a dramatic reduction in the curve to an asymptotic shape, followed by an overshoot in the recovery. Values of $v't'$ as calculated from

the wall heat flux measurements are also labelled on Figure 19 (at $y/\delta = 0.0$). The wall values and the profile measurements agree very well at station 1 and in the curve. Although little data is available near the wall in the recovery section, the values of $v't'$ seem to rise above the wall heat flux values, especially for station 10. This may perhaps be seen more clearly on Figure 20 where $v't'$ has been normalized on wall heat flux (q'') rather than the potential velocity at the wall (U_{pw}) and the wall-to-freestream temperature difference ($T_w - T_\infty$). The profiles at station 1 and within the curve approach unity near the wall, while the profiles in the recovery section seem to overshoot. It is believed that the profiles overshoot, then turn down and approach unity as the wall is approached. This raises the question of whether it is physically realistic for the cross-stream heat flux, $v't'$, to increase beyond the wall heat flux when no reversal in the sign of v and t is observed. A possible explanation may be found in the time-averaged energy equation. The applicable equation, neglecting the molecular conduction term, $\alpha \partial t / \partial y$, is given by

$$u \frac{\partial t}{\partial x} + v \frac{\partial t}{\partial y} = - \frac{\partial(v't')}{\partial y} \quad (8)$$

If $v't'$ is to increase above the wall heat flux, the term on the r.h.s. of the above equation must be negative. The term $v \partial t / \partial y$ is expected to be negative since $v > 0$ (boundary layer is growing), and $\partial t / \partial y < 0$ (wall is heated). Since u is always positive, the condition that must be satisfied for a positive gradient in $v't'$ is

$$\frac{\partial t}{\partial x} < - \frac{v}{u} \frac{\partial t}{\partial y} < 0 \quad (9)$$

i.e., the mean temperature, t , must momentarily decrease with x for a particular y . This condition could occur in the recovery section. You, et al. (1986) and Simon, et al. (1980) have shown that the Stanton number

increases in the recovery, implying an increase in the heat transfer coefficient, h . An increase in h with x implies a decrease in the temperature near the wall, i.e., $\partial t / \partial x < 0$. Physically, eddy diffusion of heat in the cross-stream direction is increasing at the expense of convection of heat in the streamwise direction.

Profiles of turbulent Prandtl number, Pr_t , are shown on Figure 21. The data show some unavoidable scatter, but it is seen that Pr_t decreases in the curve below the station 1 values. This is inconsistent with the observations of Gibson and Verriopoulos (1984) who stated that Pr_t rises within the curve for $y/\delta < 0.4$ (though this was not conclusive in the data due to scatter) and with the observations of You, et al. (1986) and Simon, et al. (1980) who saw Pr_t rise in the log-linear region. The reason for this inconsistency is not presently known although it should be noted that the second and third references present Pr_t values deduced from the mean temperature and velocity profiles which apply to the turbulent core whereas the present values and the Gibson and Verriopoulos values were measured in the wake.

High TI Case (TI=2.0%):

The high turbulence case was obtained by inserting a grid at the entrance to the contraction section as discussed in section A. Merging of the boundary layers occurred at station 6 and beyond due to the rapid growth of the boundary layer on the unstable concave side for the high TI case. The data taken at station 6 and beyond were therefore disqualified.

Shear stress profiles are presented on Figure 22. The higher turbulence intensity has the effect of increasing the shear stress throughout the boundary layer. This is expected. The profiles immediately assume an asymptotic shape within the curve for $y/\delta < 0.5$, unlike the low TI

case where an evolution of profiles was observed. The asymptotic profile for the low TI case is also plotted on Figure 22, and is seen to agree well with the high TI data in the curve. A reversal in the sign of the shear stress is seen to occur in the outer part of the boundary layer, along with a slow relaxation. This reversal in sign has also been observed by Gillis and Johnston (1983) for more strongly curved flows. The cause of this reversal is not yet understood, but is thought to be linked to the sudden drop in the production of shear stress in the curve. This is presently under study.

The effect of turbulence intensity on t' is shown on Figure 23. The flat plate values are seen to be greater than the low turbulence values by approximately 60%. This increase is completely eliminated by station 4, however, where the values agree with the asymptotic profile of the low TI case. This dramatically illustrates the dominance of curvature over turbulence intensity.

The dominance of curvature is again illustrated by the $u't'$ profiles shown on Figure 24. Although the flat plate values for the high TI case are 150% higher than the corresponding values for the low TI case, a profile agreeing with the asymptotic profile for the low TI case is achieved by station 4. The effect of curvature is remarkable.

Profiles of $v't'$ are given on Figure 25. The usual trends are observed. Values of $v't'$ higher than the corresponding low TI values are seen at station 1, while an asymptotic profile agreeing with the asymptotic profile for the low TI case is achieved in the curve. $v't'$ is seen to react faster than $u't'$ and t' , however, achieving an asymptotic shape by station 3 instead of station 4. The profiles are seen to agree well with the wall heat flux measurements. Profiles of $v't'$ normalized on the wall heat flux

are shown on Figure 26. The station 1 values are expected to level out and approach unity near the wall.

Turbulent Prandtl number profiles are shown on Figure 27. A slight decrease in Pr_t within the curve near the wall is seen. It is interesting that in this profile the values of Pr_t become negative in the wake due to the sign reversal in shear stress, as discussed earlier. This strong variation in Pr_t indicates that Reynolds analogy is not valid.

Conclusions. The effects of curvature, recovery and turbulence intensity on turbulent boundary layer heat transfer were studied. The main conclusions are:

- (1) Profiles of $u'v'$, t' , $u't'$, and $v't'$ are reduced in the curve with an asymptotic profile being achieved by station 4. Recovery in the wake region occurs quickly, with the profiles often overshooting the flat upstream (station 1) values.
- (2) A reversal of sign in the shear stress is seen for the high TI case ($TI=2.0\%$) for $y/\delta > 0.5$. This is consistent with the observations of other researchers.
- (3) Curvature is seen to decrease the turbulent Prandtl number in the wake region. Negative turbulent Prandtl numbers were seen in the wake for the high TI case and Reynolds analogy is disqualified.
- (4) Curvature effects dominate turbulence intensity effects for the cases studied.

3. Expected Activities

This probe development has been completed. More fine tuning will, of course, be done as the probe is used in subsequent experiments.

D. Transport in a Turbulent Boundary Layer with Concave Curvature

1. Objectives

This study investigates the influence of streamwise concave curvature on momentum and heat transport in a fully turbulent boundary layer.

Parameters such as freestream turbulence intensity and acceleration, which affect the flow on gas turbine blades, will be included.

This study is directed toward a better understanding of the flow and heat transfer physics with emphasis on the recovery of the flow following concave curvature. In this region, flow visualization will be carried out. Also, the existing database of turbulence and heat transfer quantities will be extended to investigate the effect of different radii of concave curvature including the recovery behavior of momentum and heat transport.

2. Progress and Accomplishments

A fan speed unit for the present wind tunnel is currently being installed. This will allow calibrating hot wire probes for velocity and temperature measurements in-situ by changing the speed of the wind tunnel. Also, experimental data can be taken for different free-stream velocities. The speed of the wind tunnel will be directly controlled from a computer.

Literature on previous studies including basic studies and reports on experimental techniques are being reviewed.

3. Expected Activities

An experimental setup which allows incorporating the effect of flow acceleration in curved ducts of various radii of curvature is being designed which employs bendable duct walls. Merging of the boundary layers at the inner (convex) and the outer (concave) wall will be prevented by applying suction at strategic locations.

Barlow (1985) carried out a visualization study of the flow over a concave surface in a water tunnel. Roll cells which develop due to the inertial instability mechanism were visualized in the curve. The present study will continue this work by investigating the behavior of the roll cells on the flat recovery section downstream of the curve. Appropriate

flow visualization techniques will be chosen. A liquid crystal technique as used by Simmonich and Moffat (1982) allows visualization of the roll cells if they are fixed in position by vortex generators.

A liquid crystal processing method, as used by Hippensteele, Russell and Torres (1985) for turbine blades, will be considered for measuring the local heat transfer coefficient. This method uses the isotherms corresponding to the yellow color of a liquid crystal sheet on a uniform heat flux wall to determine the local heat transfer coefficient.

Also, a technique using naphthalene dissolved in methyl alcohol and sprayed on the wall (McCormack, Welke and Kelleher--1970) may be applied. Smoke techniques are being considered to observe the moving roll cells in natural flow (without vortex generators).

E. Film Cooling on Curved Surfaces

This study is concerned with the film cooling on concave and convex surfaces of constant radius of curvature. It is desired to observe the effect of the ratio of radius of curvature to half the injection hole diameter ($2r/D$ -- strength of curvature) on film cooling effectiveness. A wind tunnel and test section (discussed in previous progress reports) has been constructed for this purpose. The test section has concave and convex walls with three sets of replaceable injection holes. Each set consists of a row of holes inclined at 35 degrees to the mainflow. Hole diameters were such that $2r/D$ on the concave surface was either -57, -89, or -111. On the convex surface they were 61, 94, or 115.

Effectiveness measurements have been taken for all sets of injection geometries on both surfaces for density ratios of 2.0 and 0.95. Figure 27

shows the lateral-averaged effectiveness far downstream of injection ($x/D=40$) with a density ratio of 0.95.

Stronger convex curvature is found to enhance effectiveness at low blowing rates, M , while at high blowing rates, strength of curvature seems to diminish in importance. A blowing rate is found where an increase in its magnitude causes a decrease in effectiveness. The centrifugal force of the jet at high M causes the jet to lift off the surface. Further increase in blowing rate causes the jets to merge and blockage of the mainflow from the wall results. An increase in effectiveness is, therefore, encountered.

On the concave wall, at low blowing rates, effectiveness is virtually the same for all strengths of curvature, while at higher blowing rates, increased curvature strength raises effectiveness. An increase in blowing rate, on the concave surface always causes an increase in effectiveness; the centrifugal force of the jets impinges on the concave wall.

The flat plate study of Pedersen (1972) is included in Figure 28 for comparison.

F. End-Wall Heat Transfer

1. Introduction

This work, employing the heat-mass transfer analogy using naphthalene sublimation, is an investigation of mass (heat transfer) on the end-wall. The mass transfer technique offers much greater detail of the local transfer coefficient than if heat transfer measurements were taken directly.

2. Progress and Accomplishments

In the previous progress report, results were given for the case of $Re = 1.4 \times 10^5$ (based on chord length of the cascade) and boundary layer thickness of $\delta = 0.592$ in. This is referred to as case 1. In this update,

contour plots are given for two additional test cases plus some revealing one-dimensional heat transfer plots for the endwall region.

Test cases 2 and 3, shown in Figures 29 and 30, respectively, were conducted under the following conditions: case 2 - $Re = 1.42 \times 10^5$, $\delta = 1.147$ in. and case 3 - $Re = 8.86 \times 10^4$, $\delta = 0.461$ in. A comparison between cases 1 and 2 shows the effect of an increased boundary layer thickness while comparing cases 1 and 3 shows the Re dependence. Note that the data is presented as a ratio of the local mass transfer on the endwall to the mass transfer that would be found if no turbine blades were present (pure flat plate situation). Although the contour maps indicate differences in heat transfer between the three cases of up to ~ 25% for certain regions, the data averaged across the passage shows virtually no differences (see Figure 31).

Two one-dimensional plots are also informative. First, Figure 32 shows the variation in heat transfer at locations upstream from the leading edge of a turbine blade. Note the two local maxima in the graph showing the effects of the inner vortex (higher maximum) and the main horseshoe vortex (smaller maximum). Figure 33 illustrates how the heat transfer coefficient changes across the passage. The extreme drop in heat transfer occurs where the endwall flow separates to climb the suction surface and become entrained in the passage vortex, while the maximum near the suction surface is due to the formation of a suction side corner vortex.

3. Expected Activities

The writing of a formal paper on the endwall phase of this project is currently underway while the development of equipment to measure mass transfer on turbine blades continues.

G. Near-End-Wall Heat Transfer

1. Objectives

The present study is to investigate the performance of film cooling on the convex surface of the turbine blade through two rows of injection holes in the near-end-wall region. Several parameters which do not occur at the two-dimensional flow region do affect the performance of film cooling. These parameters include: lower free stream velocities and higher turbulent intensity inside the boundary layer, the passage vortex traveling from the concave side of the adjacent blade, horseshoe vortex generated from the leading edge, deflected mainstream direction, and the plugged injection hole of the second row. The passage vortex, which plays a dominant role, sweeps the coolant from the convex surface and leaves a triangular region without film protection.

Test facilities and detailed arrangements of injection holes and sampling taps are shown in Figures 34 and 35, respectively. The injection hole, half blocked by the end wall, is plugged to assure the uniformity of secondary jet through each injection hole. Results with lower density ratio, $R=0.96$, were reported last year. Results on the convex surface with higher density ratio, $R=2.0$, are presented herein.

2. Progress and Accomplishments

Presently, the approaching velocity which is measured at 12.9 cm from the leading edge of the turbine blade is 9.8 m/s. The boundary layer thickness, δ_{99} , at the same location is 2 cm and the turbulence intensity, Tu , of the freestream is 1.2%. The Reynolds number, Re_{∞} , is based on the freestream velocity, $U_{\infty}=17.8$ m/s, at the injection hole of the first row and the diameter of the injection hole. Figures 36 through 38 show the values of the average film cooling effectiveness at blowing rates of $M=0.5$,

1.02, and 1.47, respectively. The solid symbols on the right axis are values of average effectiveness measured in the two-dimensional flow region at midspan of the blade. The open and solid circular symbols are mapped into the convex surface of the turbine blade and form the boundaries of region B and region C in Figures 39 and 41. The distributions of average effectiveness at density ratios of $R=2.0$ and 0.96 are shown in Figures 39 and 40, respectively.

Region C, where coolant is swept from the surface by the effect of the passage vortex, is the unprotected region. In region B, the values of average effectiveness at each downstream location decrease linearly to zero as the elevation, H , moves from the upper boundary toward the lower boundary. As expected, the area of the region C slightly decreases with increasing blowing rates and the upper boundary of the region B stays the same as the blowing rate changes. Comparison of the distribution of average effectiveness between two different density ratios $R=2.0$ and $R=0.96$ is shown in Figure 41. Boundaries of region B move slightly toward the end wall. Comparison of values of the average effectiveness is shown in Figure 42.

3. Expected Activities Next Contract Year

Complete results on the concave surface with higher density ratios will be presented next year.

		CASE 1	CASE 2	CASE 3	
R	--	90	210	90	(cm)
U_{pw}	--	16.32	17.12	15.83	(m/s)
I.I.	--	0.65	0.65	1.85	(x)
δ/R at B.O.C.	--	0.03	0.013	0.036	
θ/R at B.O.C.	--	0.0036	0.0016	0.0036	
δ/R at E.O.C.	--	0.04	0.019	0.042	
θ/R at E.O.C.	--	0.0054	0.0025	0.0048	

* B.O.C. -- Beginning of Curvature

* E.O.C. -- End of Curvature

Table 1. Descriptors of CASES 1, 2 & 3

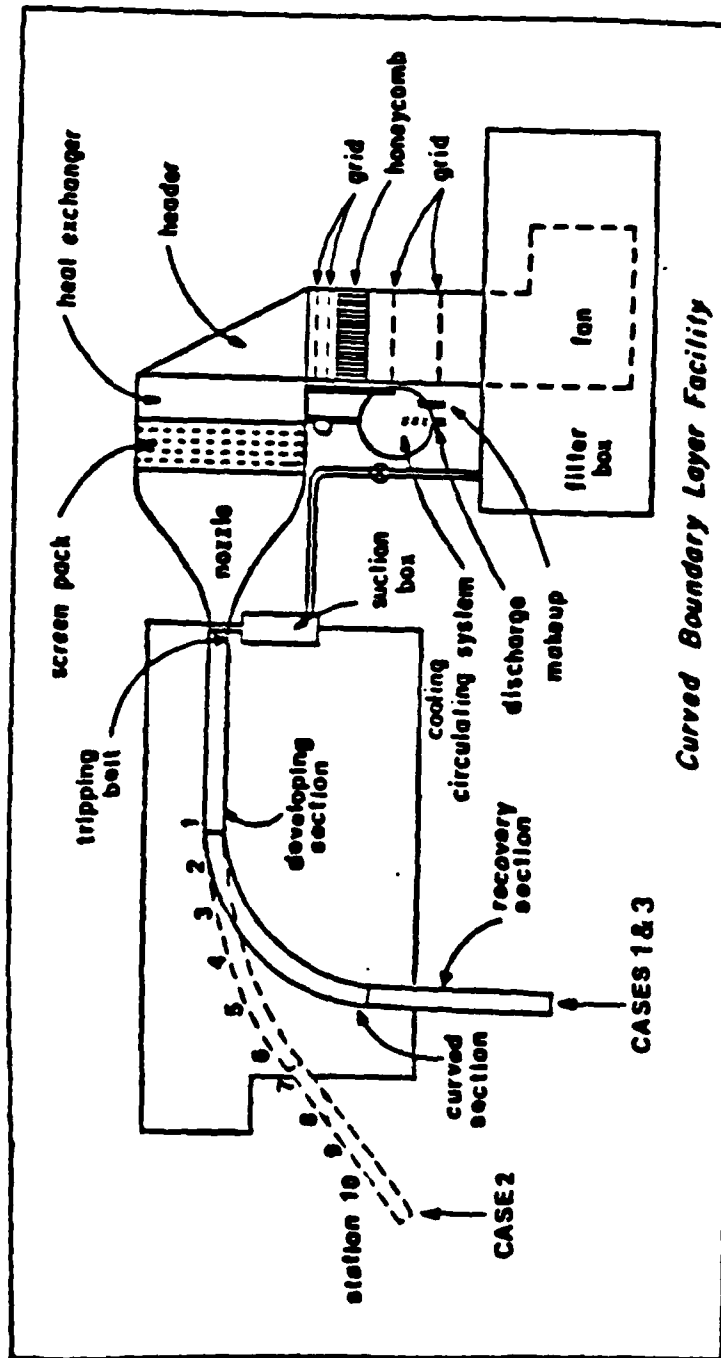


Figure 1. Plan View of the Curved Boundary Layer Facility

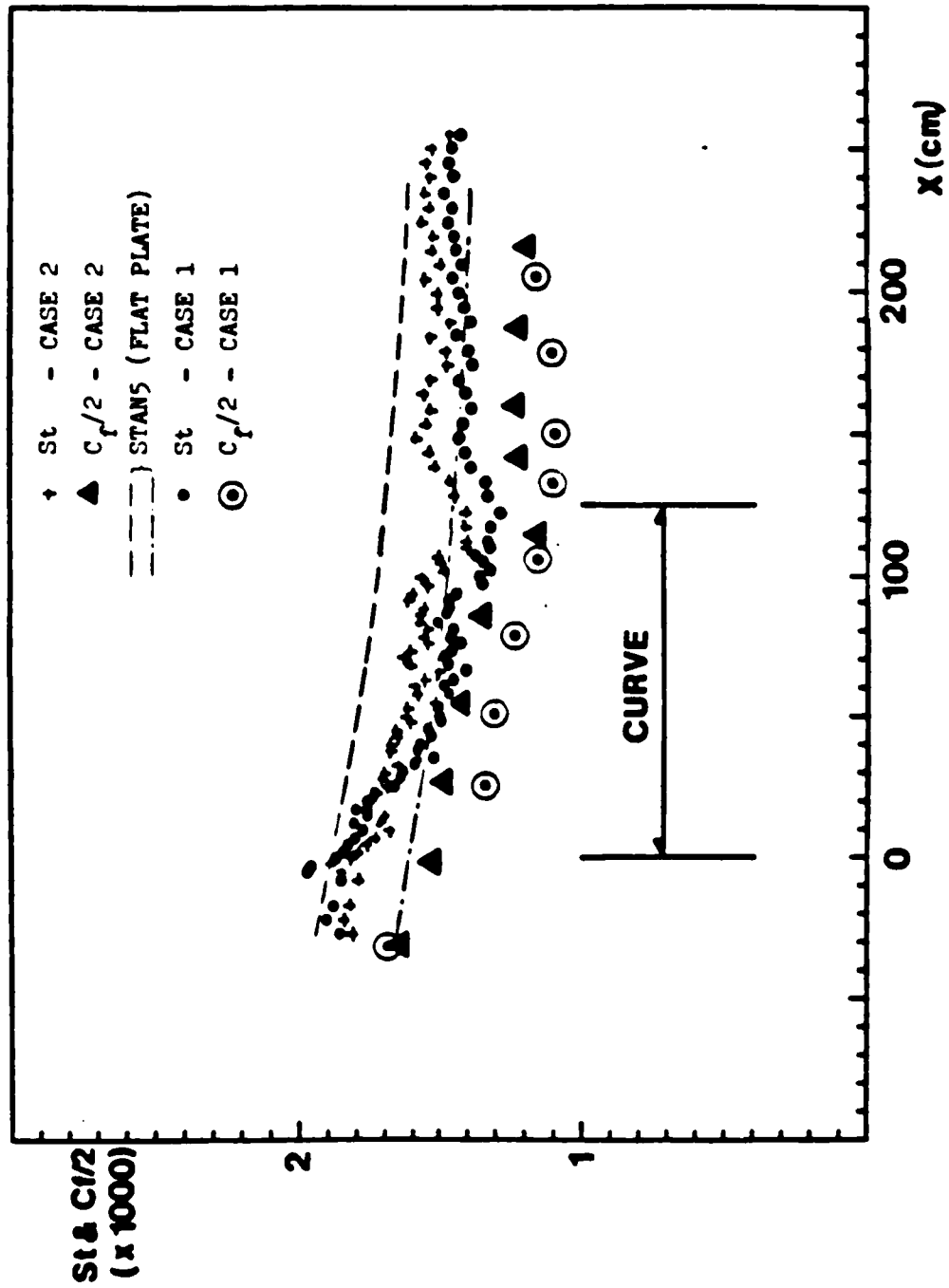


Figure 2. Stanton Number & Skin Friction Coefficient vs. Streamwise Distance, Comparison between CASES 1 & 2

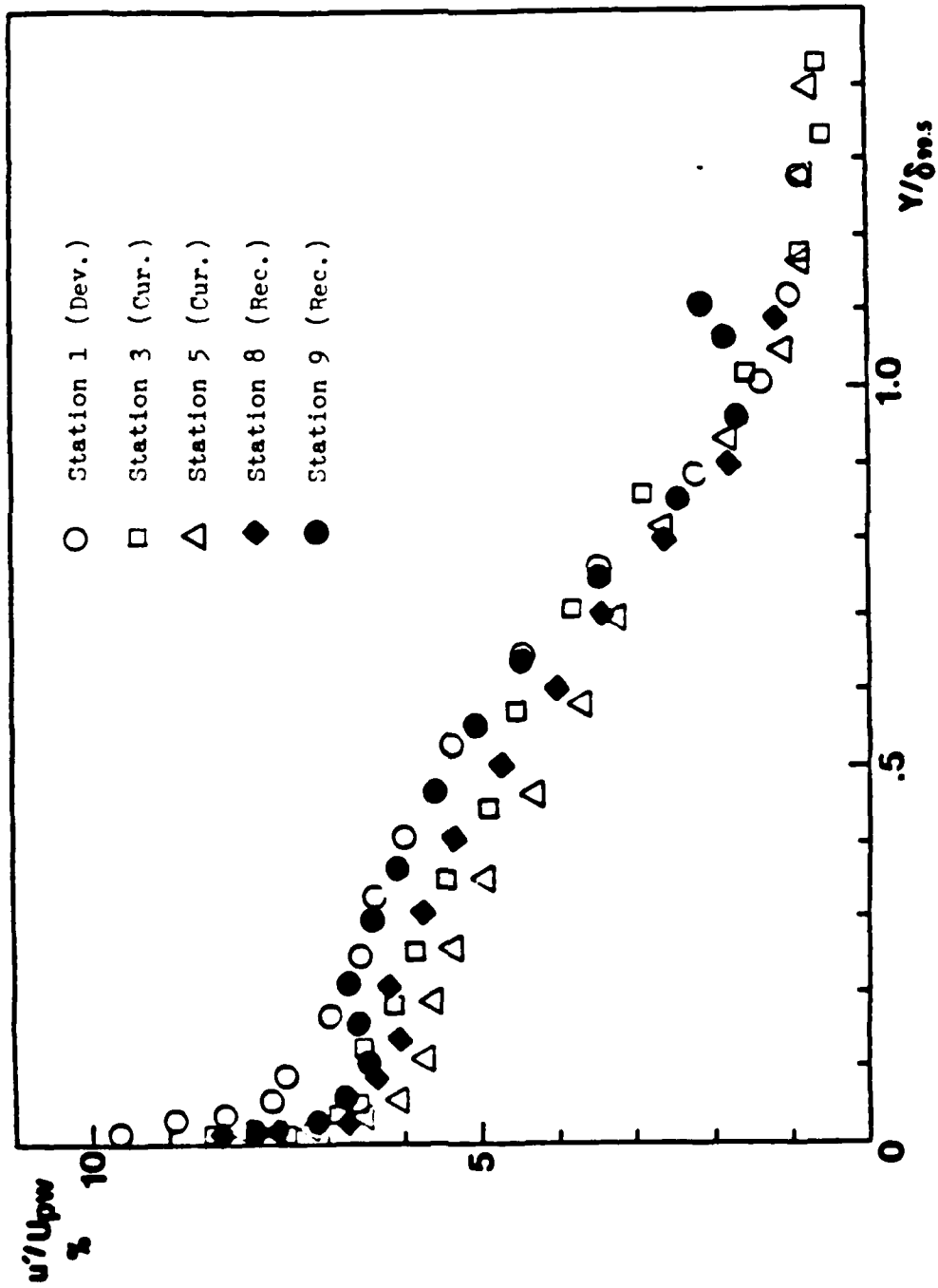


Figure 3. Streamwise-normal Turbulence Intensity Profiles,
CASE 1 -- The Base Case

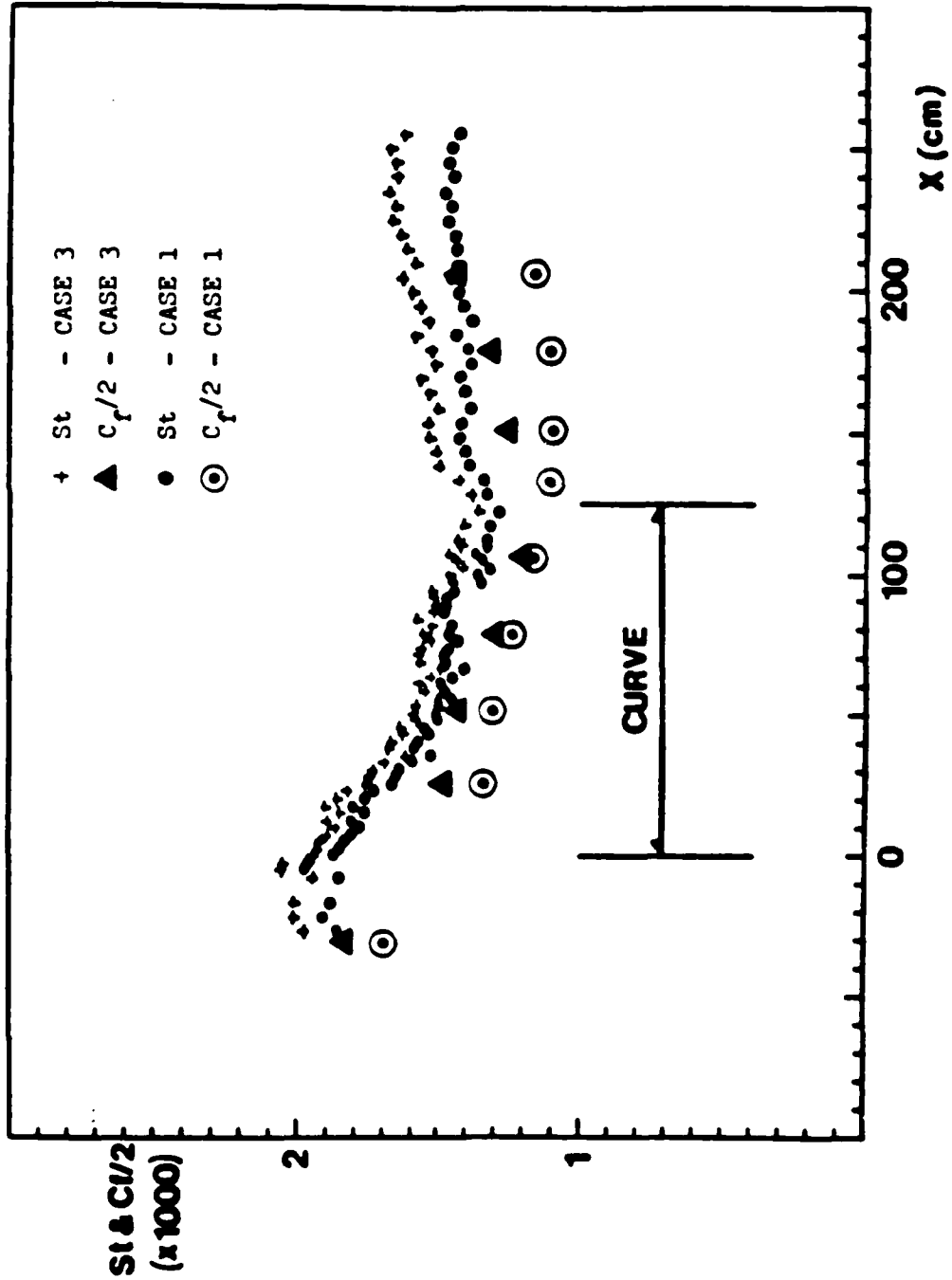


Figure 4. Stanton Number & Skin Friction Coefficient vs. Streamwise Distance, Comparison between CASES 1 & 3

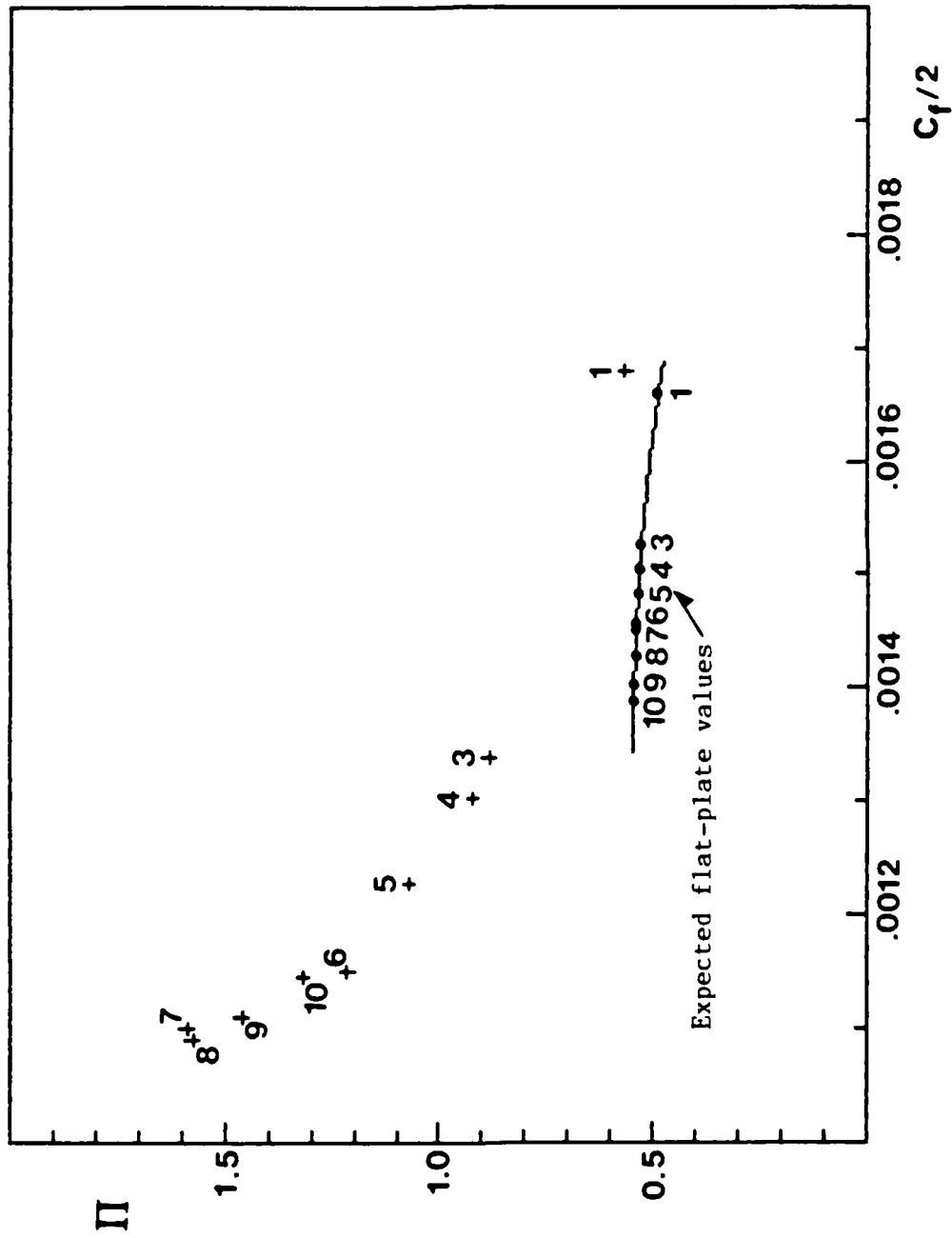


Figure 5. Wake Parameter vs. Skin Friction Coefficient, CASE 1

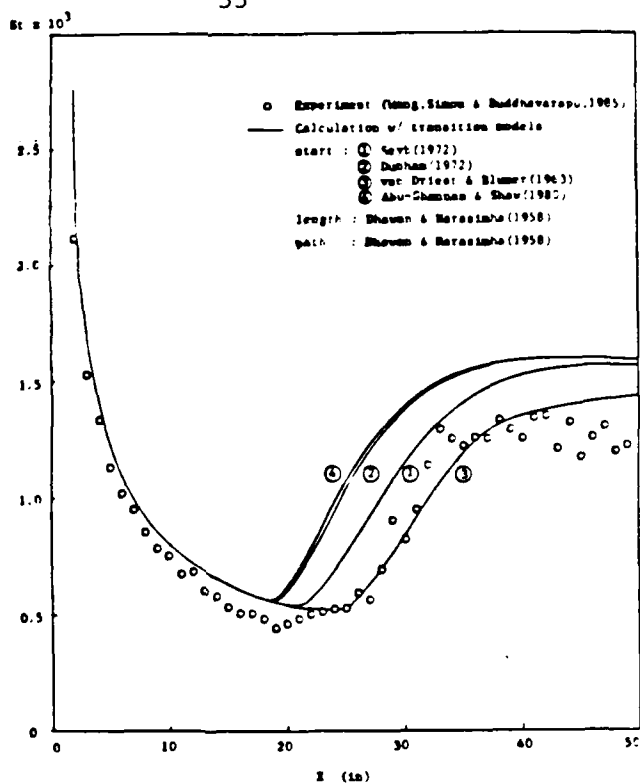


Figure 6(a). Comparison of transition start models
 $U_\infty = 34$ m/s, $TI = 0.68\%$, flat plate

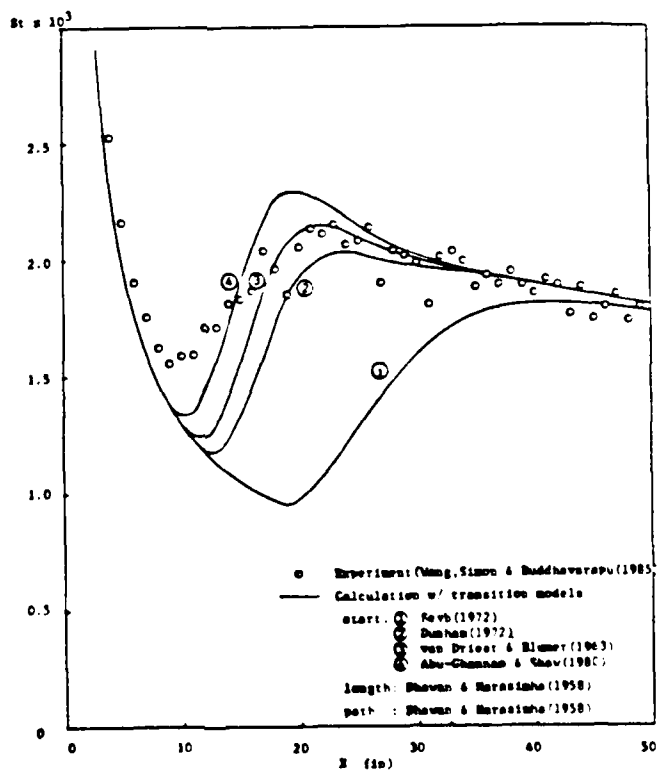


Figure 6(b). Comparison of transition start models
 $U_\infty = 13$ m/s, $TI = 2\%$, flat plate

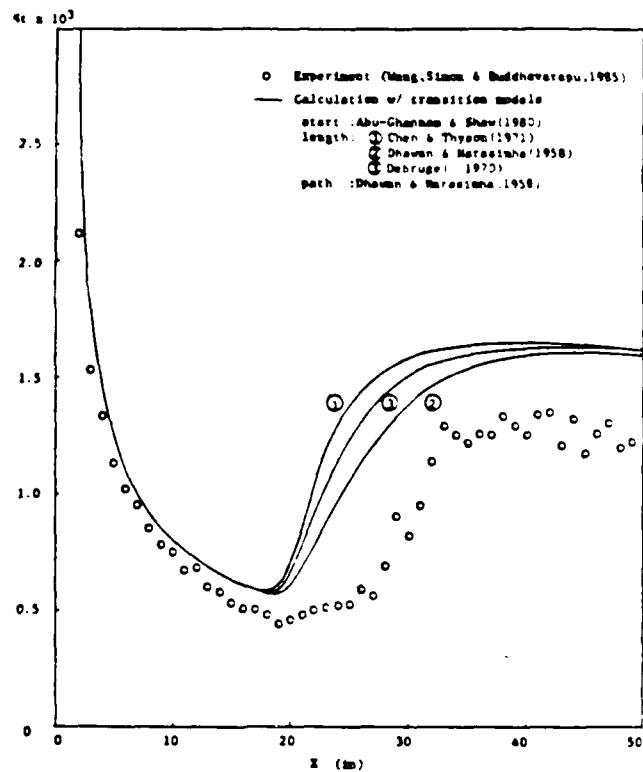


Figure 7(a). Comparison of transition length models
 $U_\infty = 34 \text{ m/s}$, $TI = 0.68\%$, flat plate

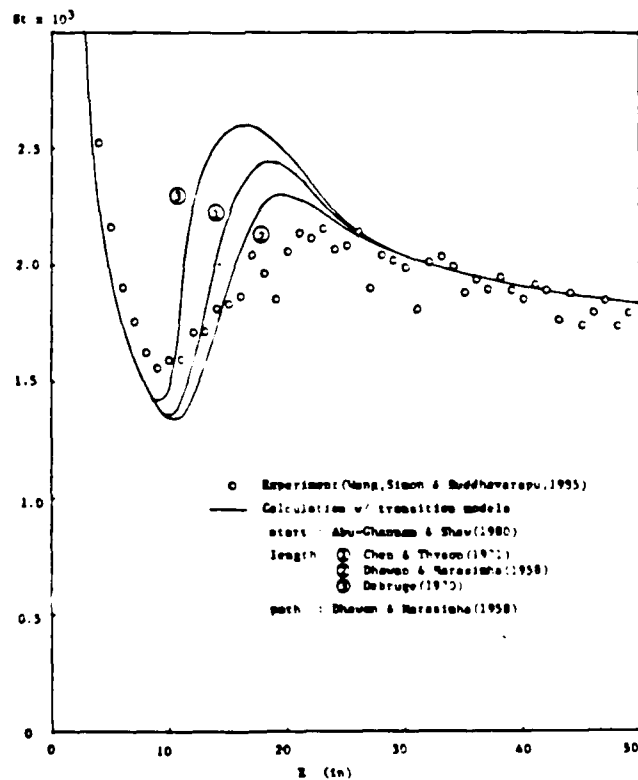


Figure 7(b). Comparison of transition length models
 $U_\infty = 13 \text{ m/s}$, $TI = 2\%$, flat plate

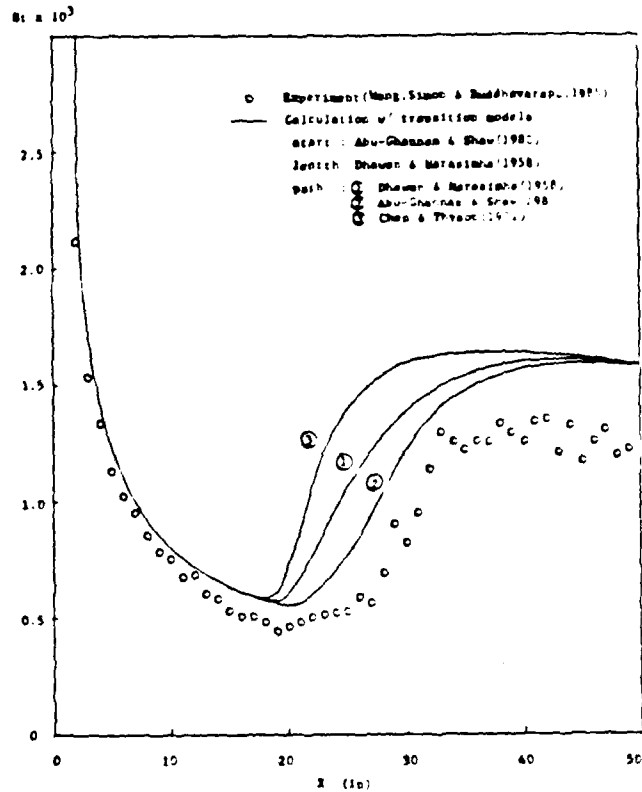


Figure 8(a). Comparison of transition path models
 $U_\infty = 34$ m/s, $TI = 0.68\%$, flat plate

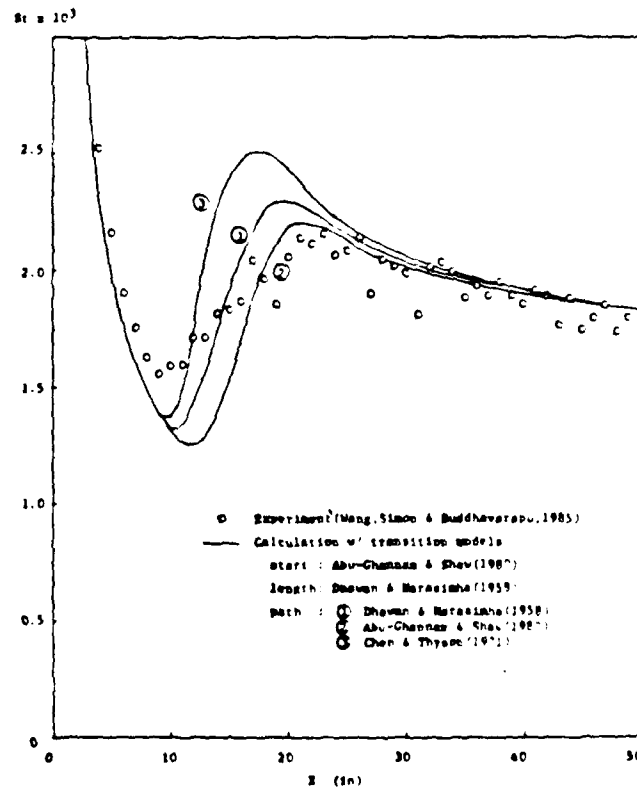


Figure 8(b). Comparison of transition path models
 $U_\infty = 13$ m/s, $TI = 2\%$, flat plate

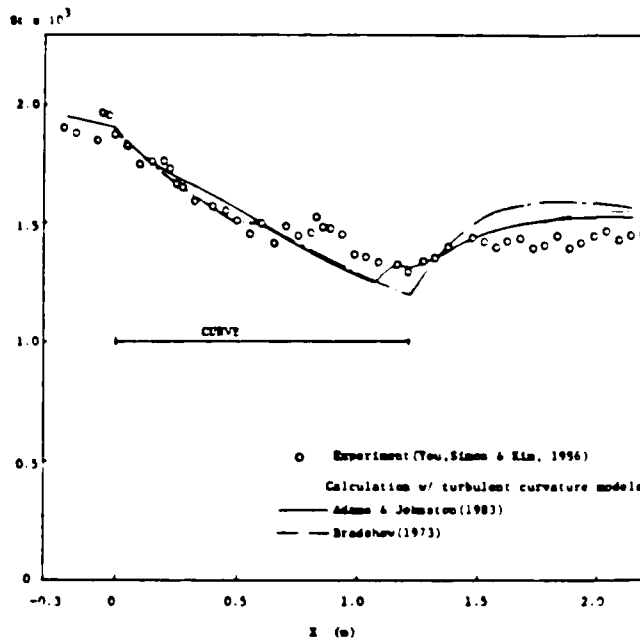


Figure 9(a). Comparison of turbulent curvature models

$U_{\infty} = 16$ m/s, $TI = 0.65\%$,
 $R = 90$ cm (convex)

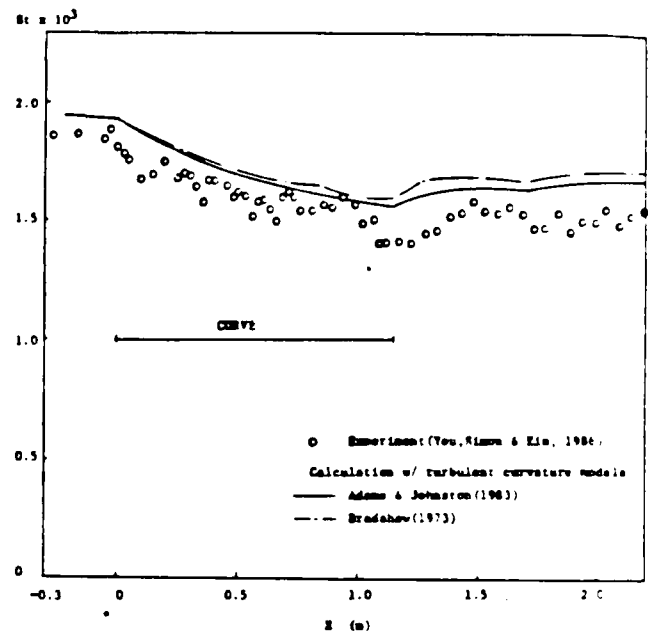


Figure 9(b). Comparison of turbulent curvature models

$U_{\infty} = 17$ m/s, $TI = 0.65\%$,
 $R = 210$ cm (convex)

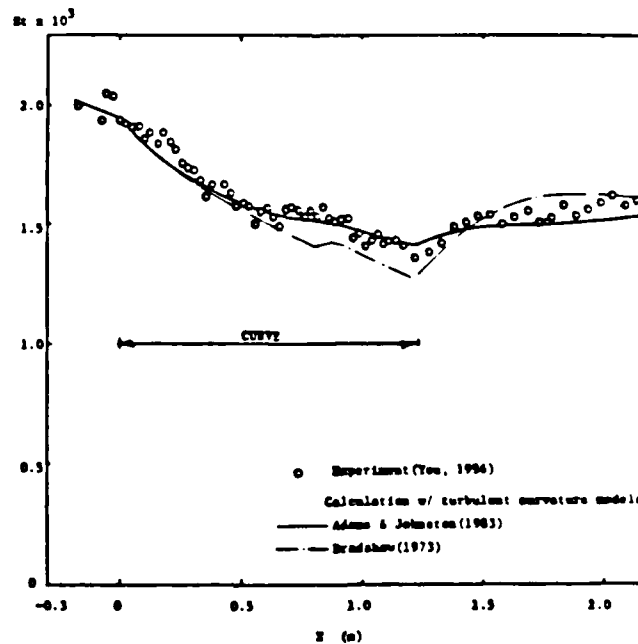


Figure 9(c). Comparison of turbulent curvature models

$U_{\infty} = 16$ m/s, $TI = 1.85\%$,
 $R = 90$ cm (convex)

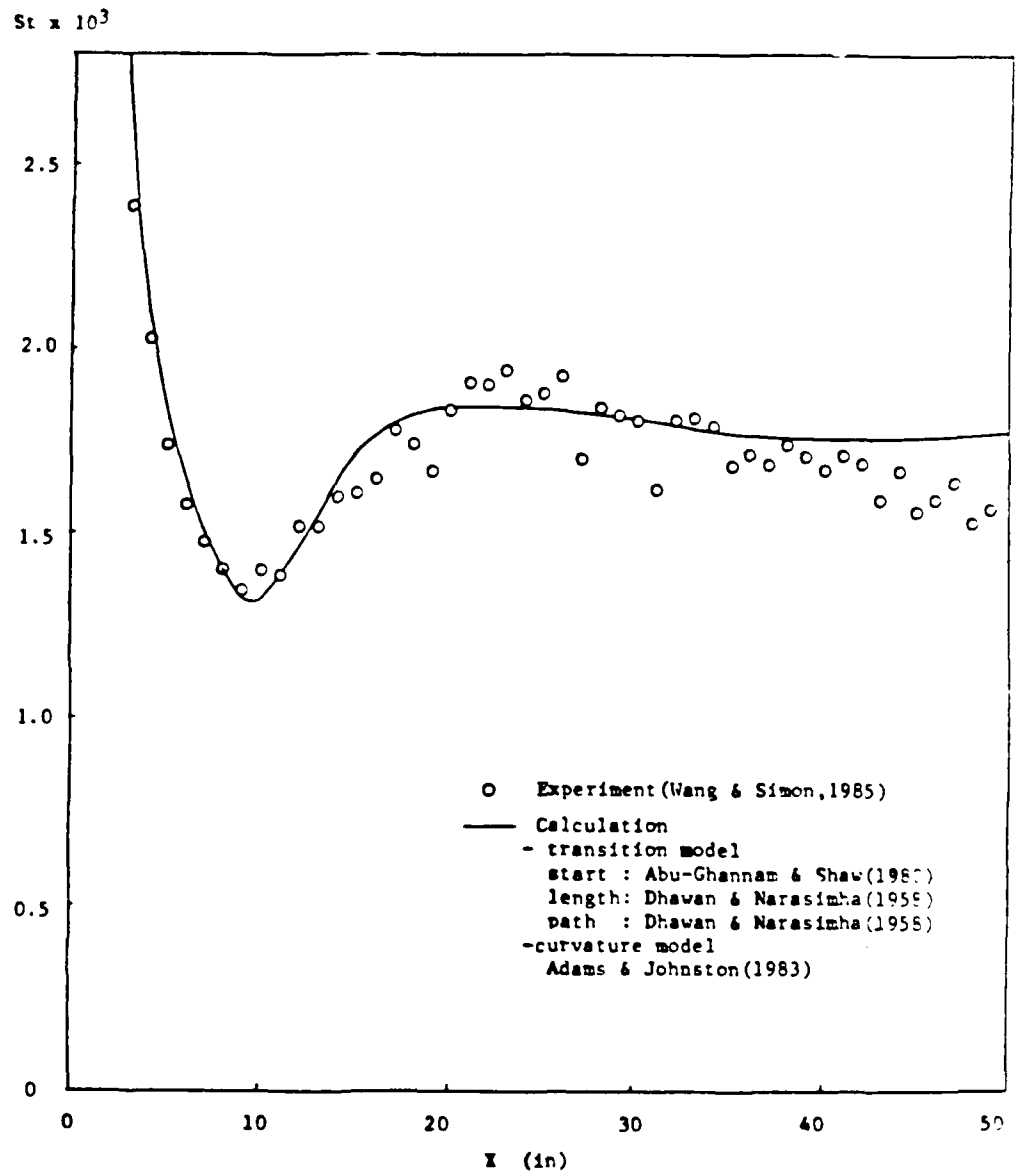


Figure 10. Calculation of convex-curved wall transition flow with transition-curvature combined model

$$U_{\infty} = 14.5 \text{ m/s}, TI = 2.0\%, R = 180 \text{ cm}$$

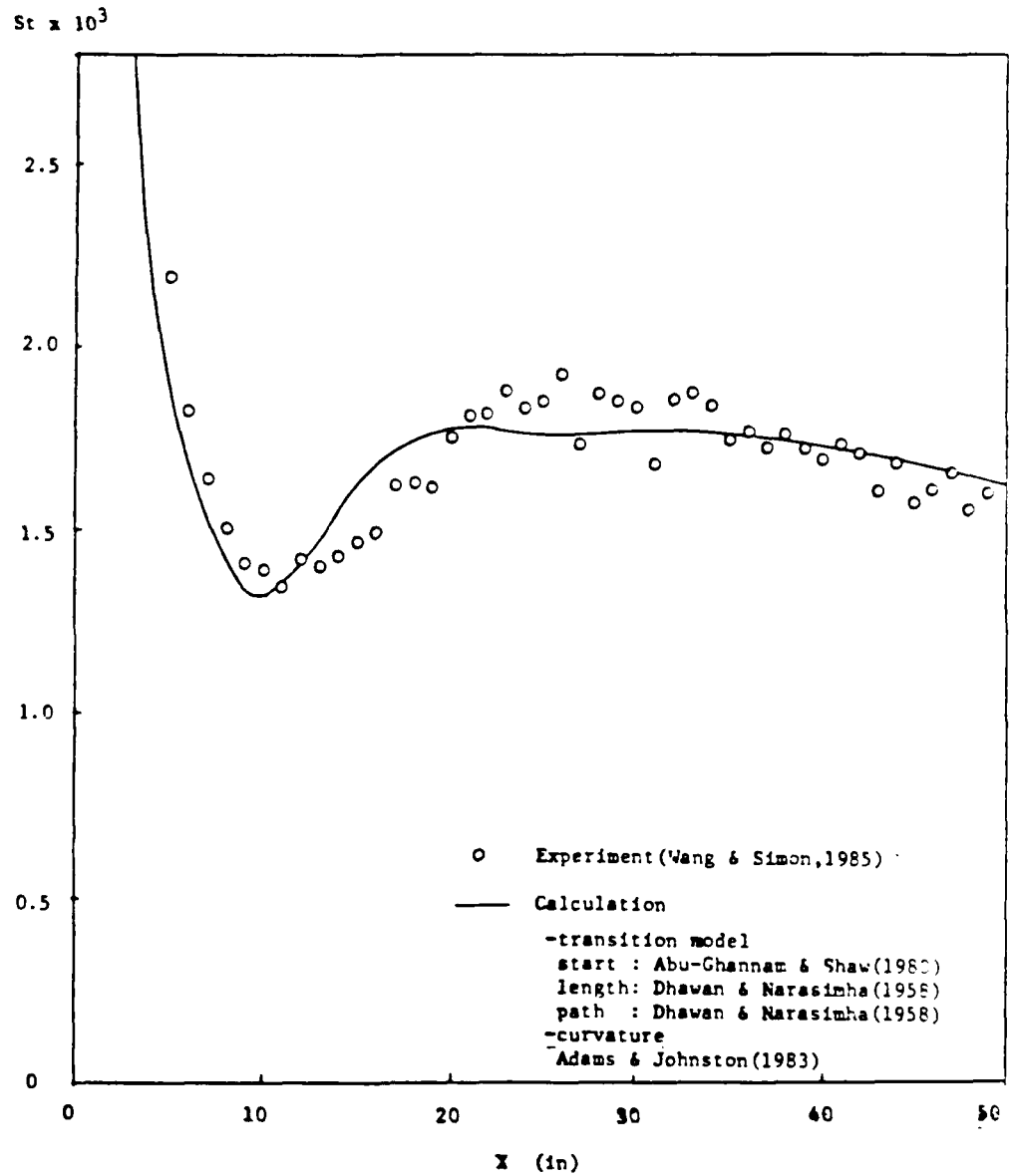


Figure 11. Calculation of transitional flow over a convex-curved wall with transition-curvature combined model

$U_\infty = 14.5$ m/s, $TI = 2\%$, $R = 90$ cm

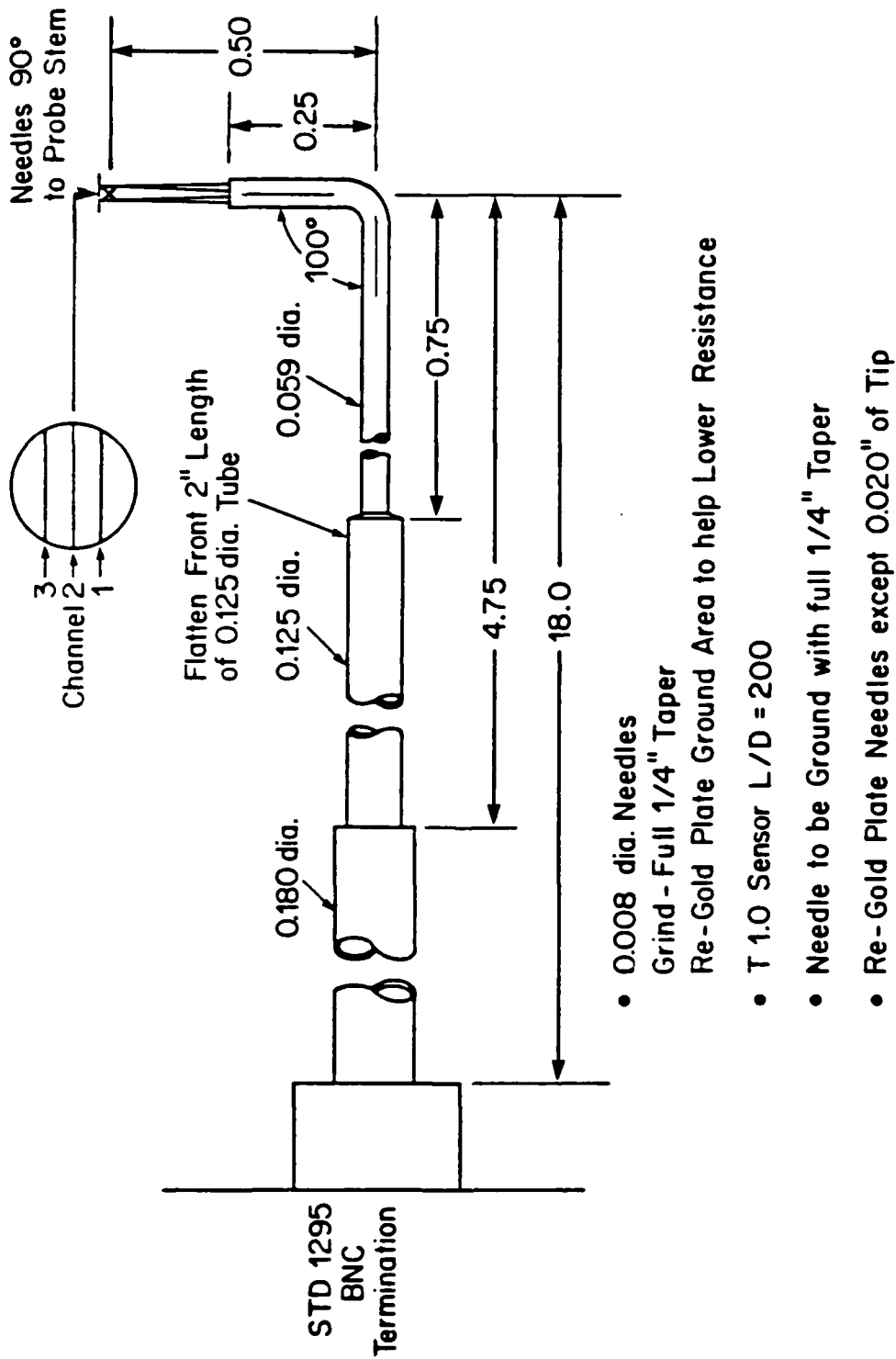


Figure 12. Schematic of probe

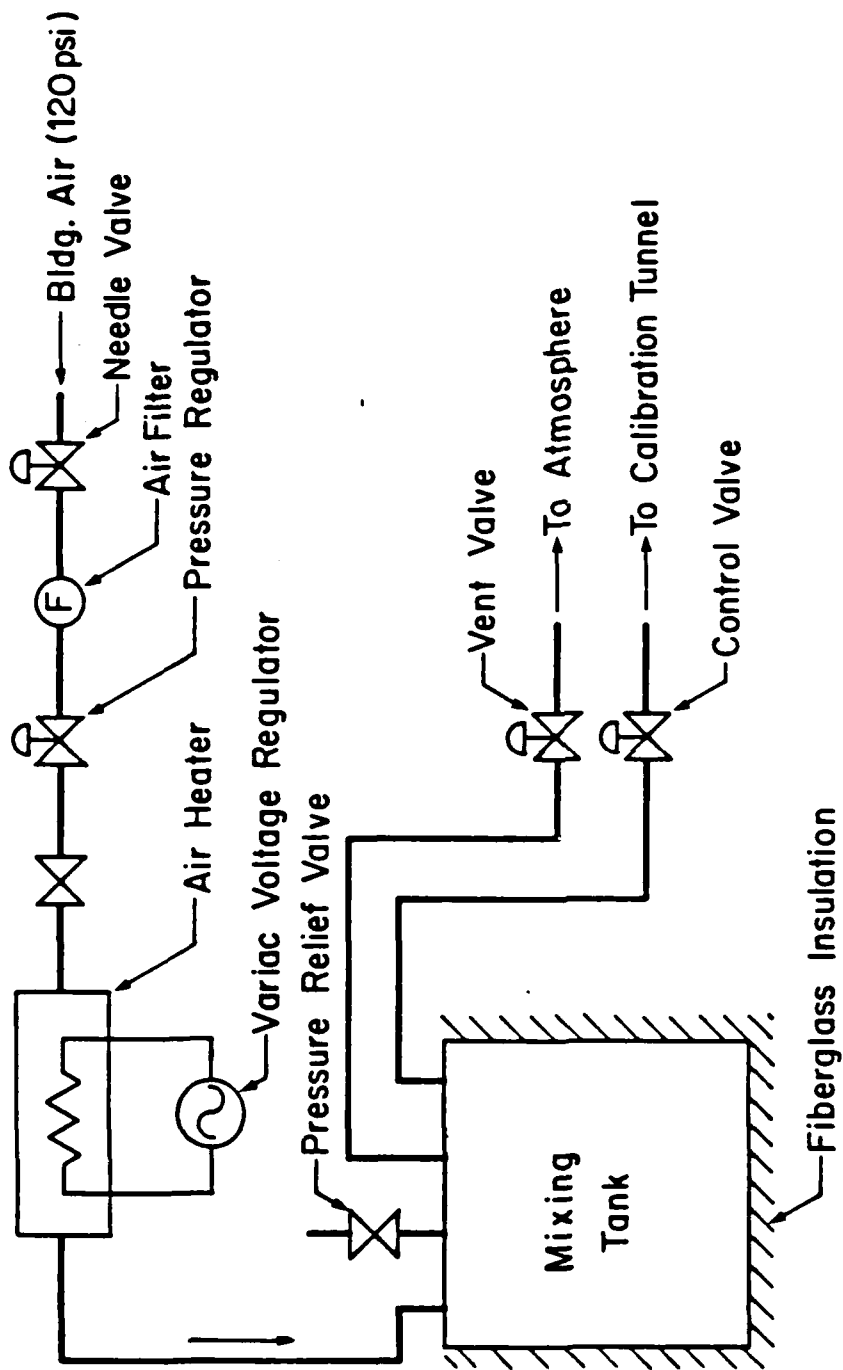


Figure 13. Schematic of calibration facility

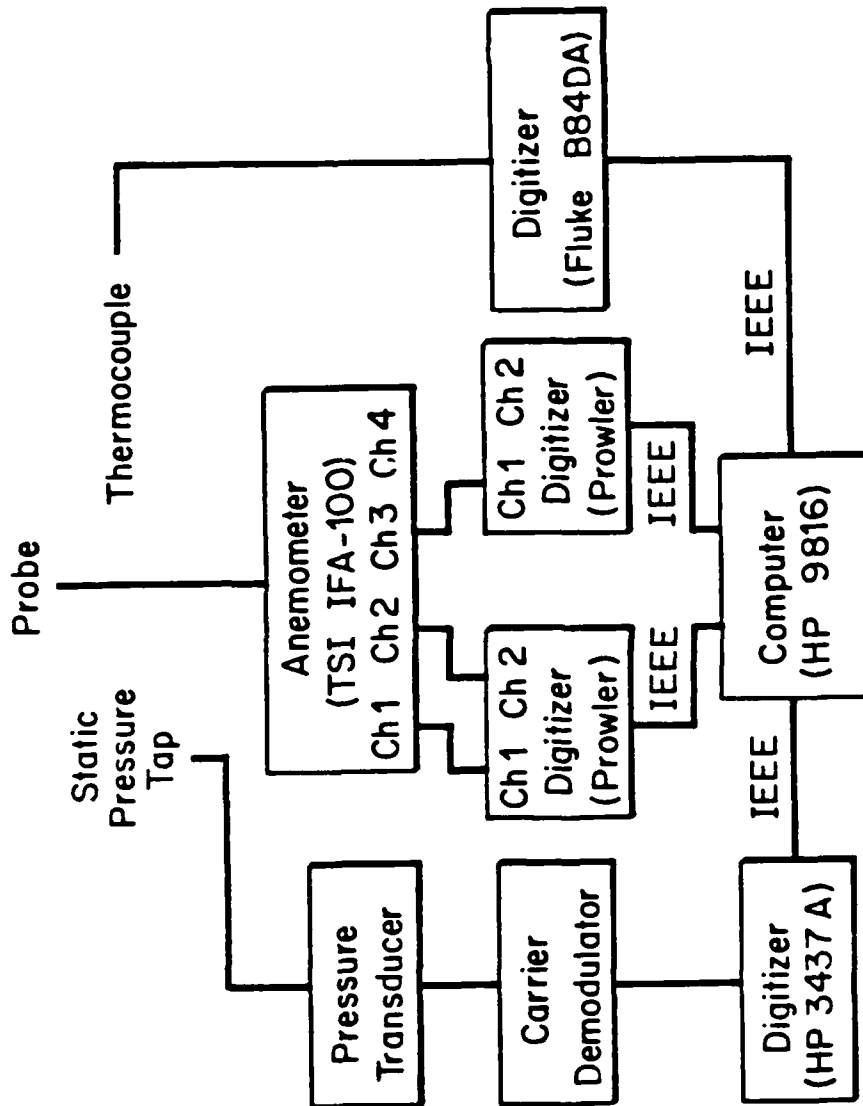


Figure 14. Set-up for calibration of probe

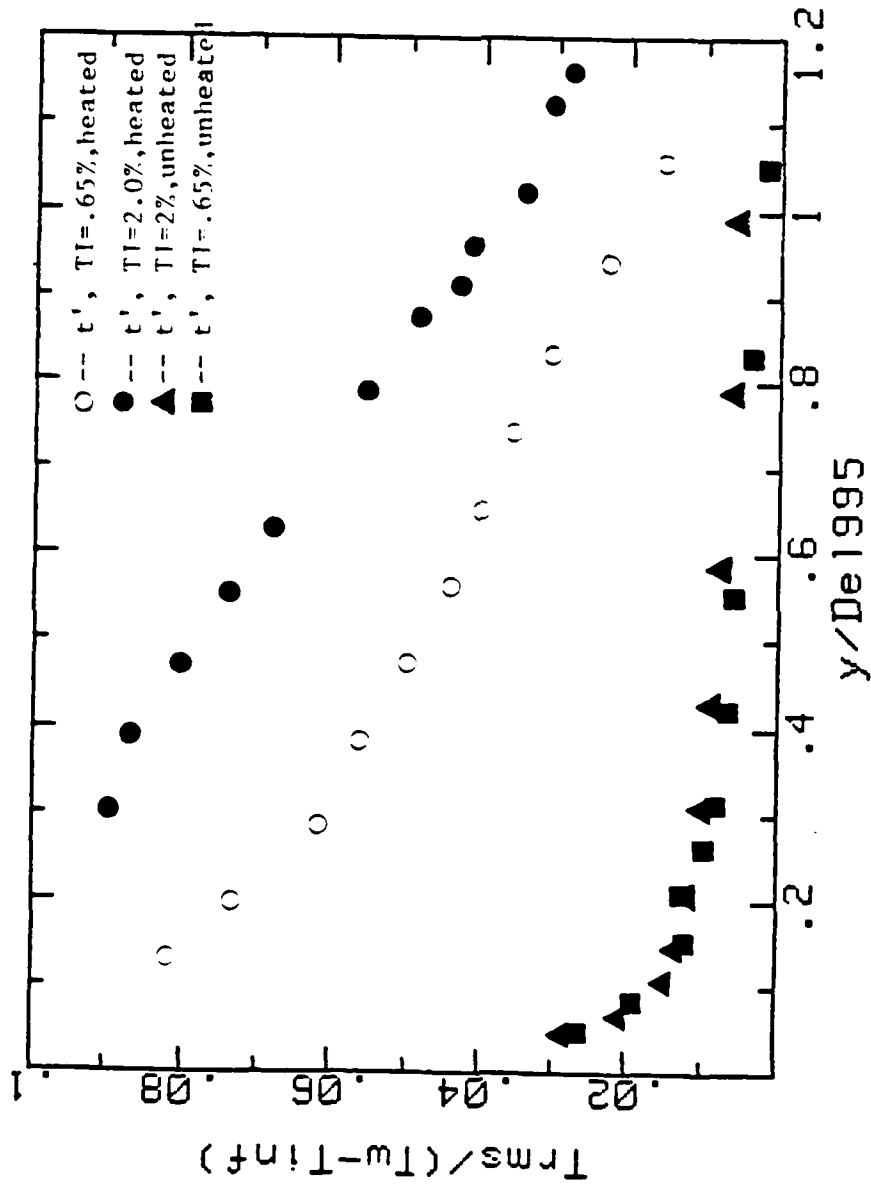


Figure 15. Comparison of apparent t' with t' taken in heated boundary layer

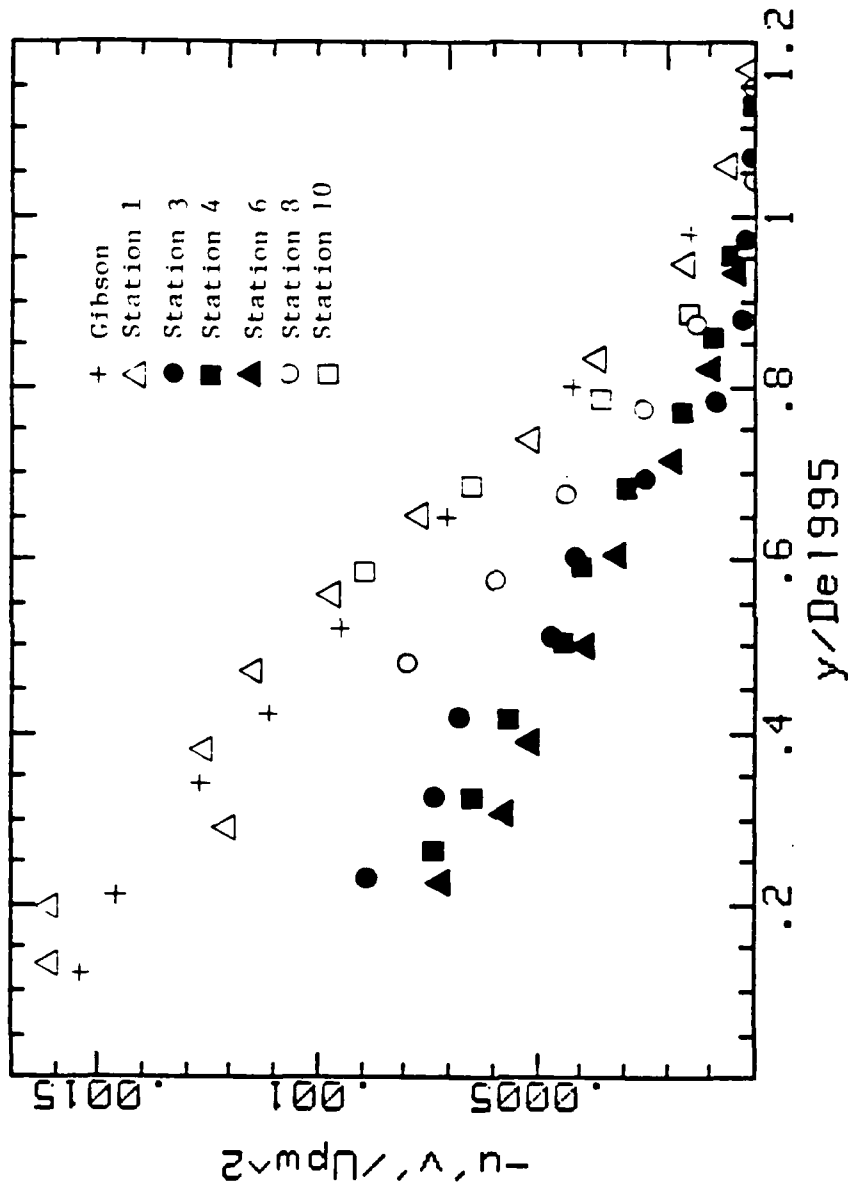


Figure 16. Shear stress profiles (TI = 0.65%)

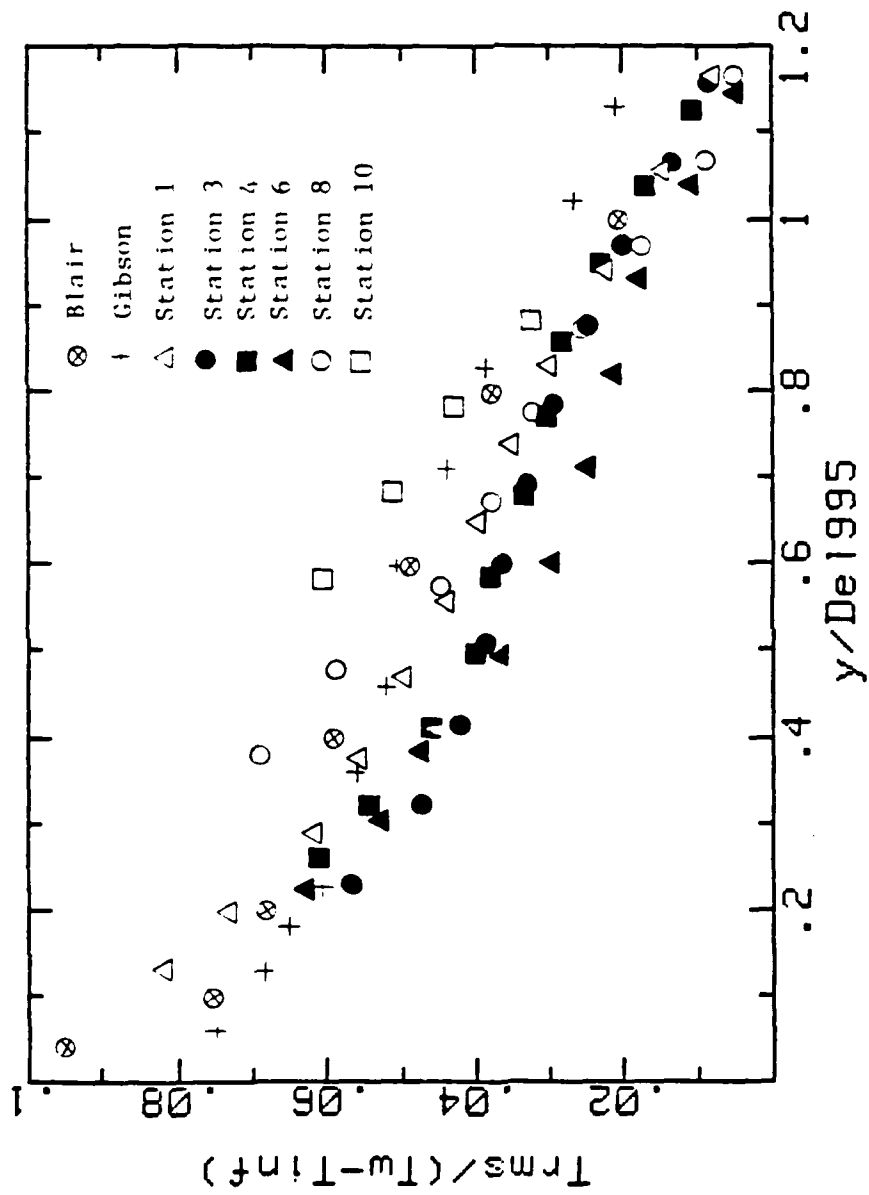
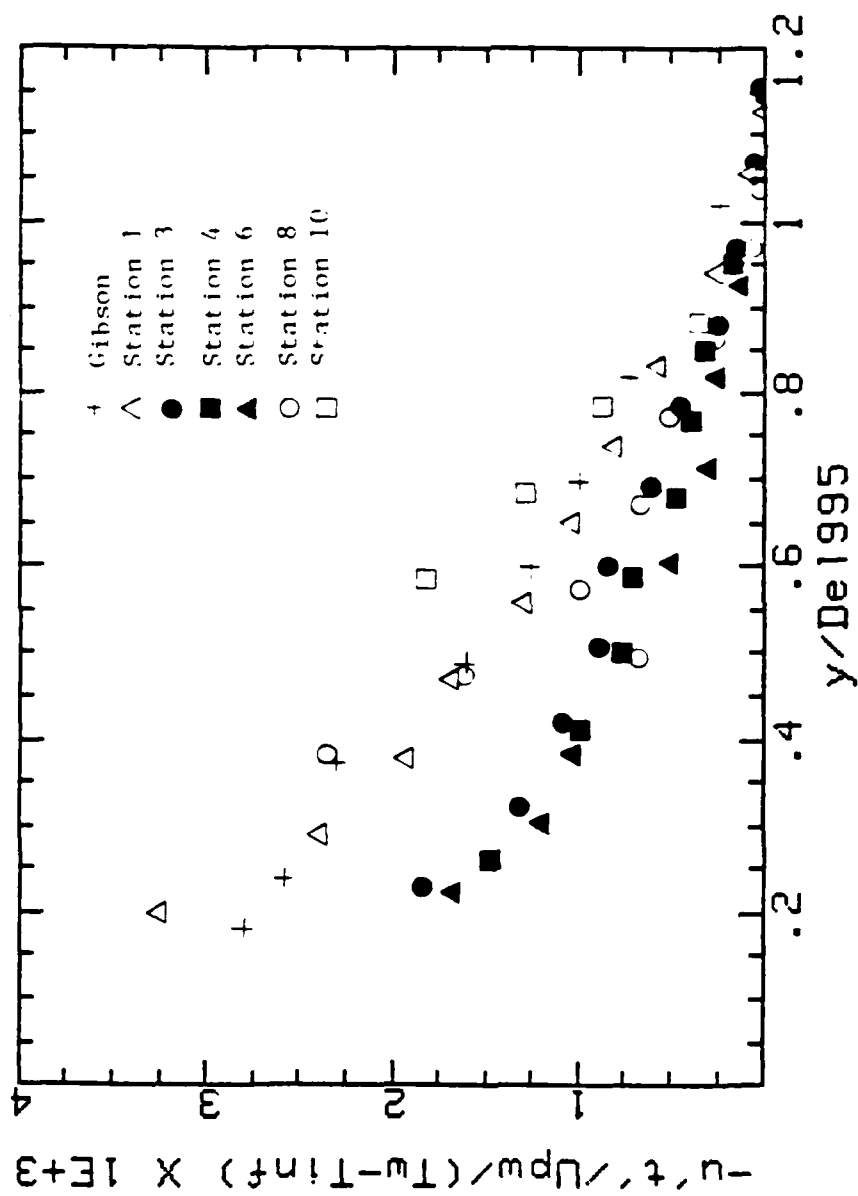
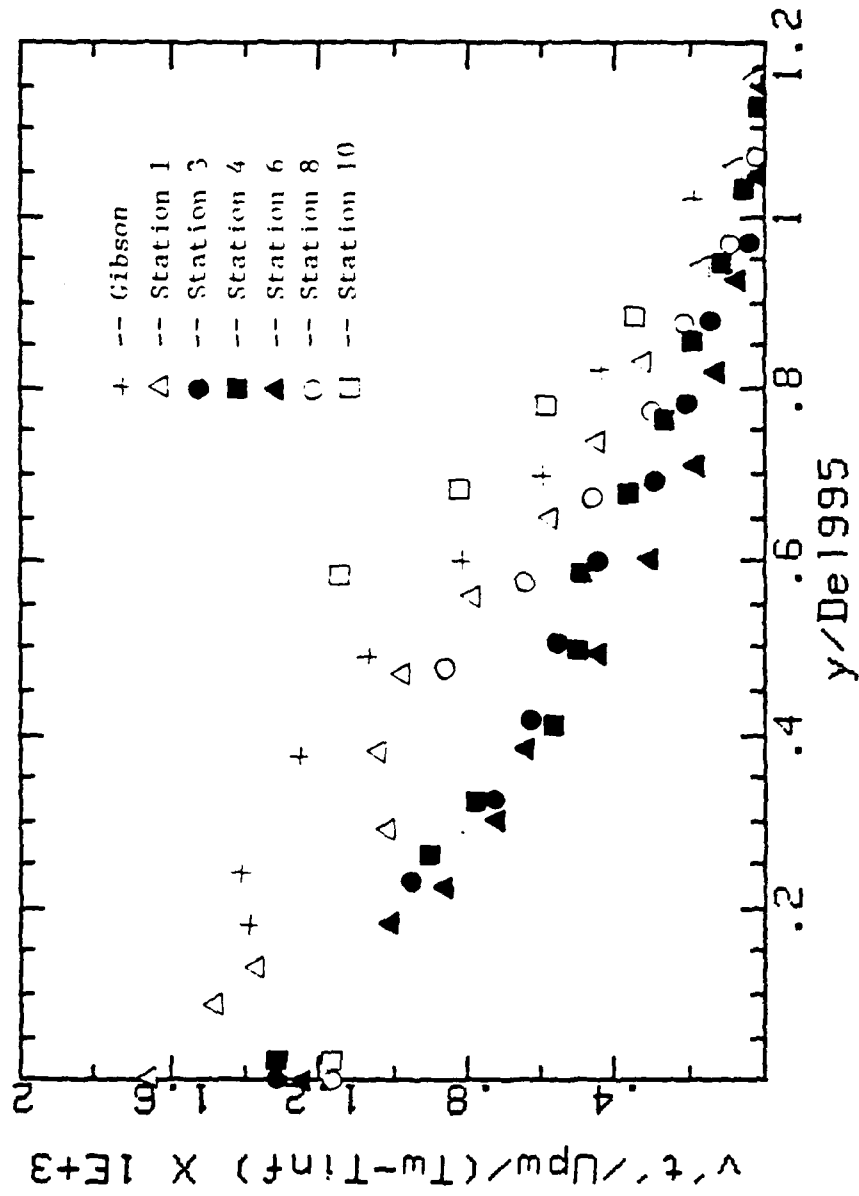


Figure 17. t' profiles ($TI = 0.65\%$)

Figure 18. $u't'$ profiles ($TI = 0.65\%$)

Figure 19. $v't'$ profiles ($Tl = 0.65\%$)

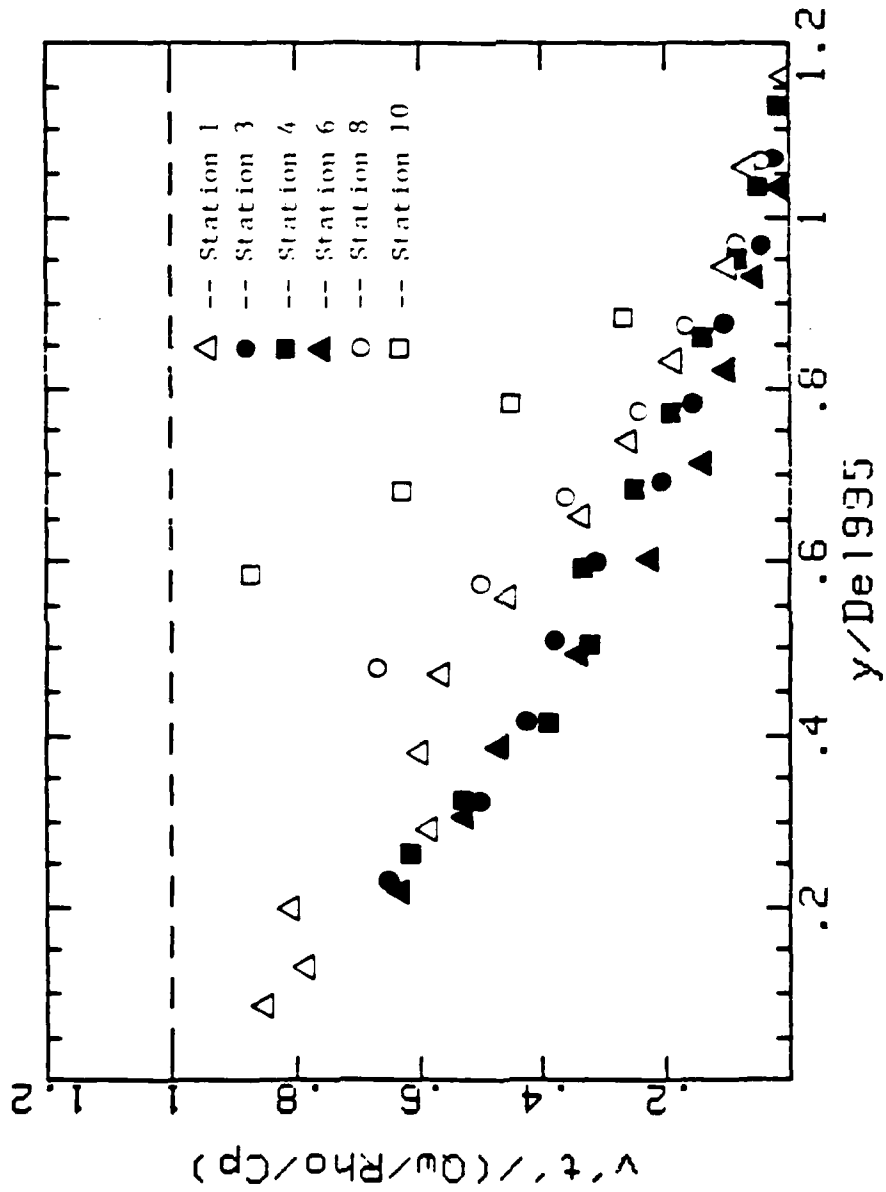


Figure 20. $v't'$ profiles normalized on wall heat flux ($TI = 0.65\%$)

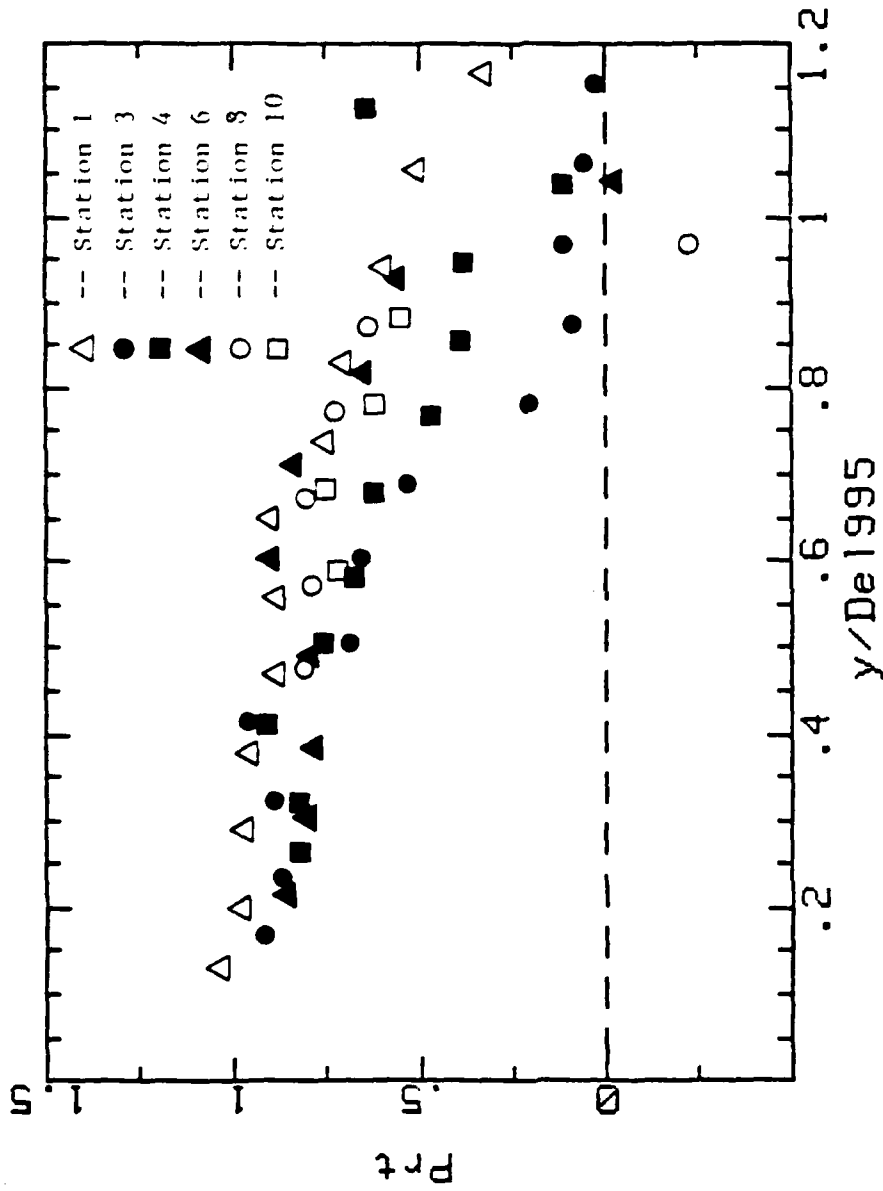
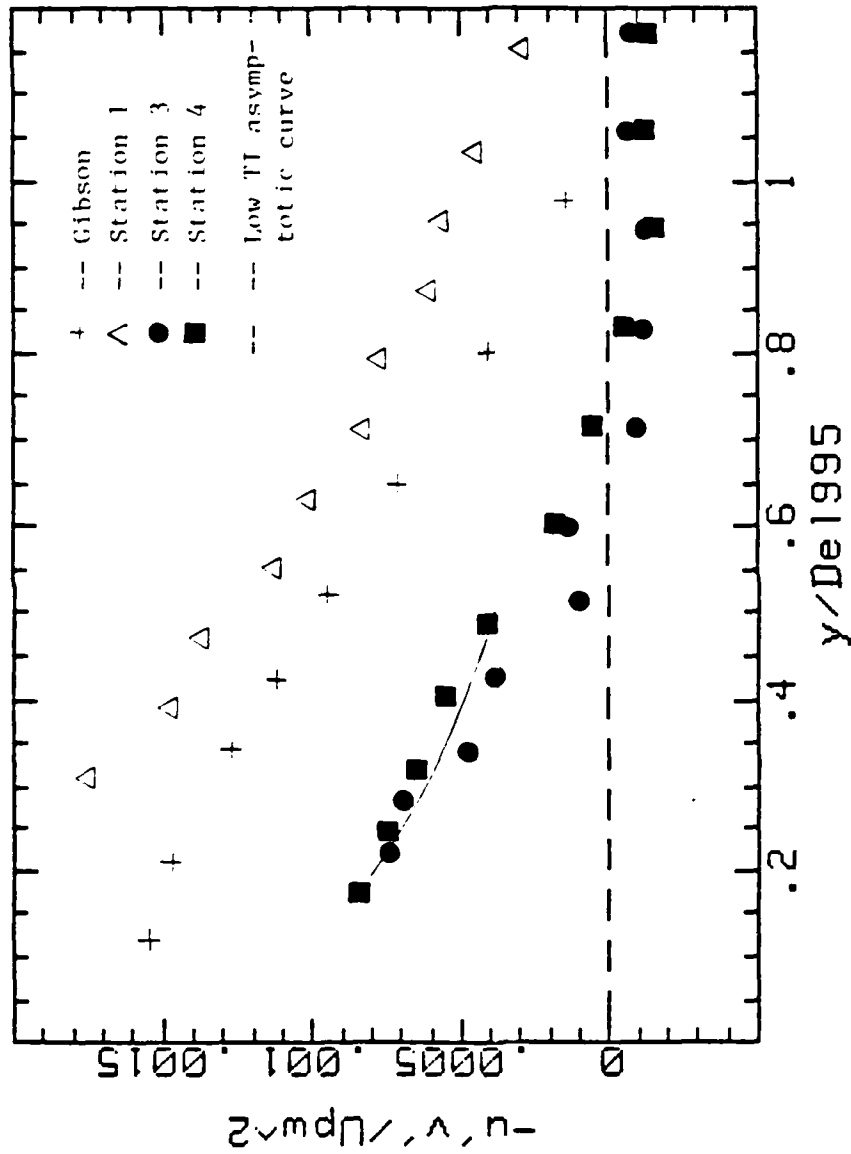
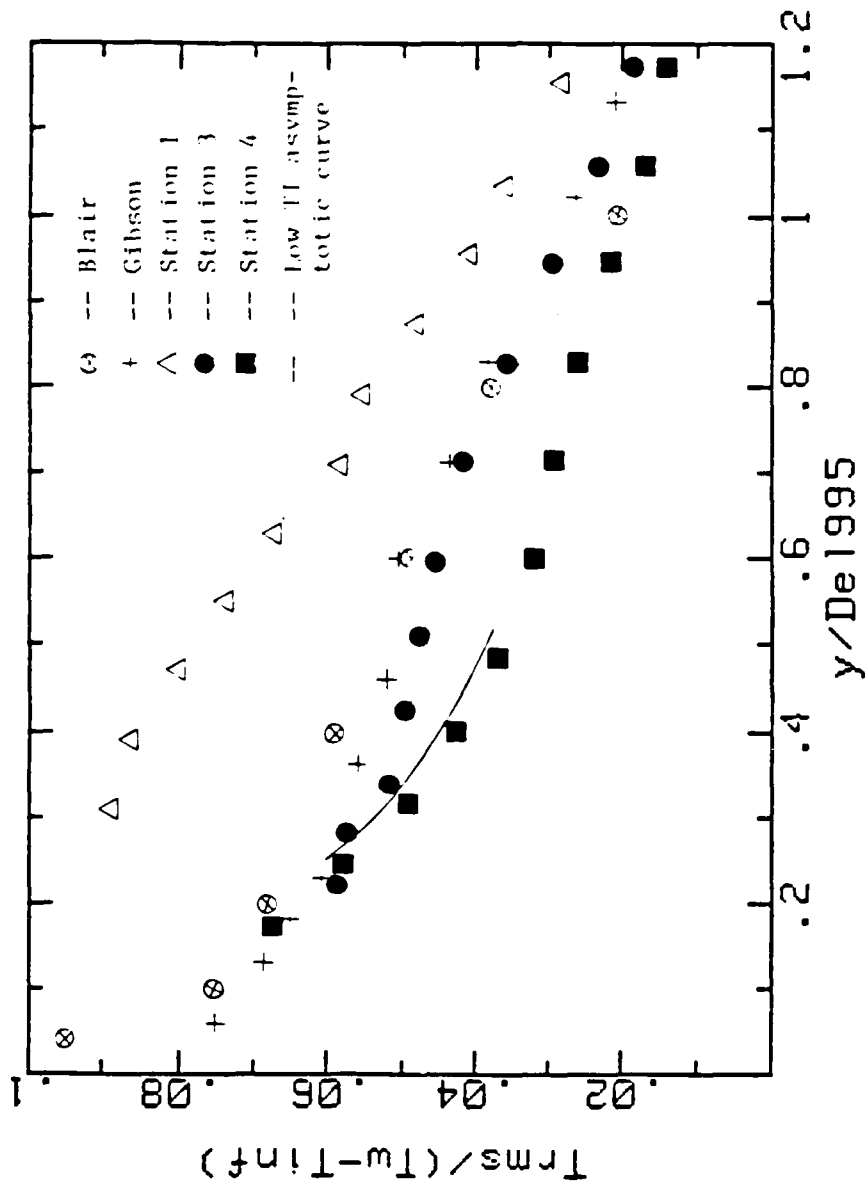
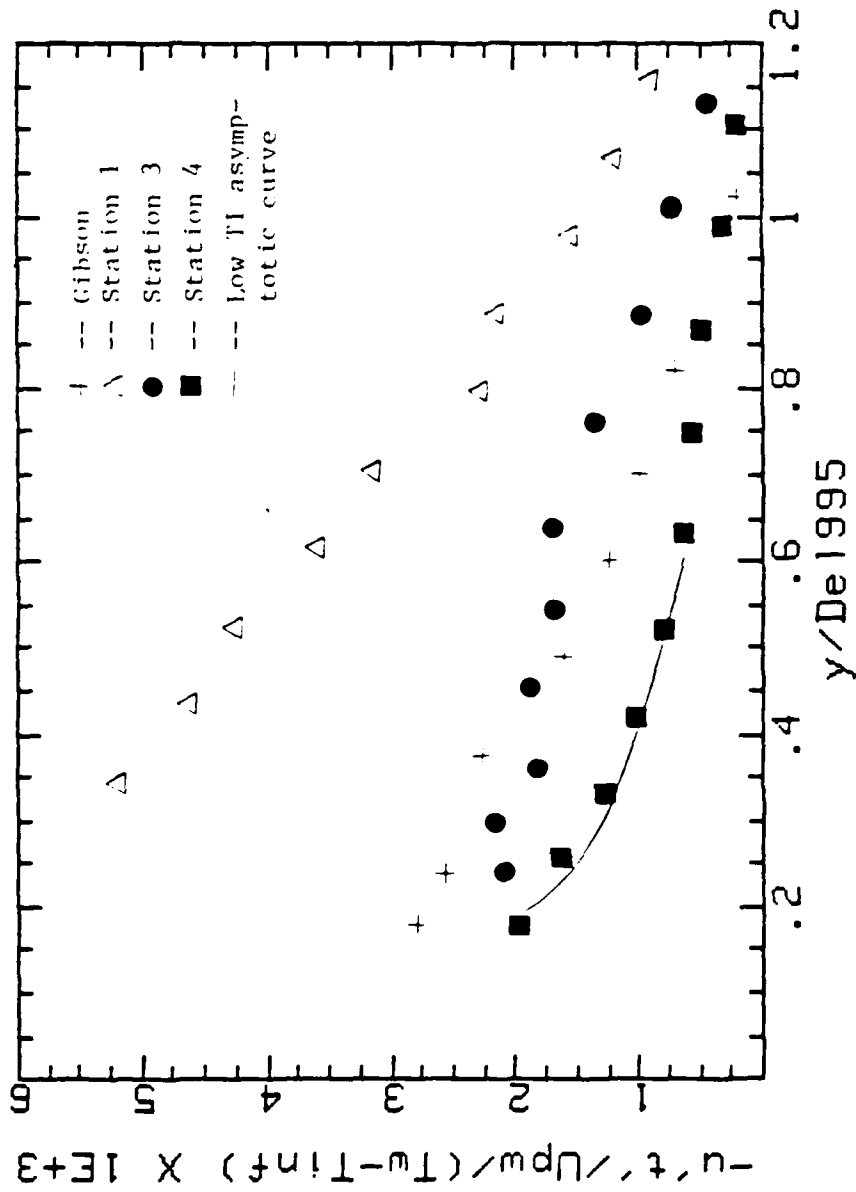


Figure 21. Turbulent Prandtl number profiles ($TI = 0.65\%$)

Figure 22. Shear stress profiles ($TI = 2.0\%$)

Figure 23. t' profiles ($TI = 2.0\%$)

Figure 24. $u't'$ profiles ($TI = 2.0\%$)

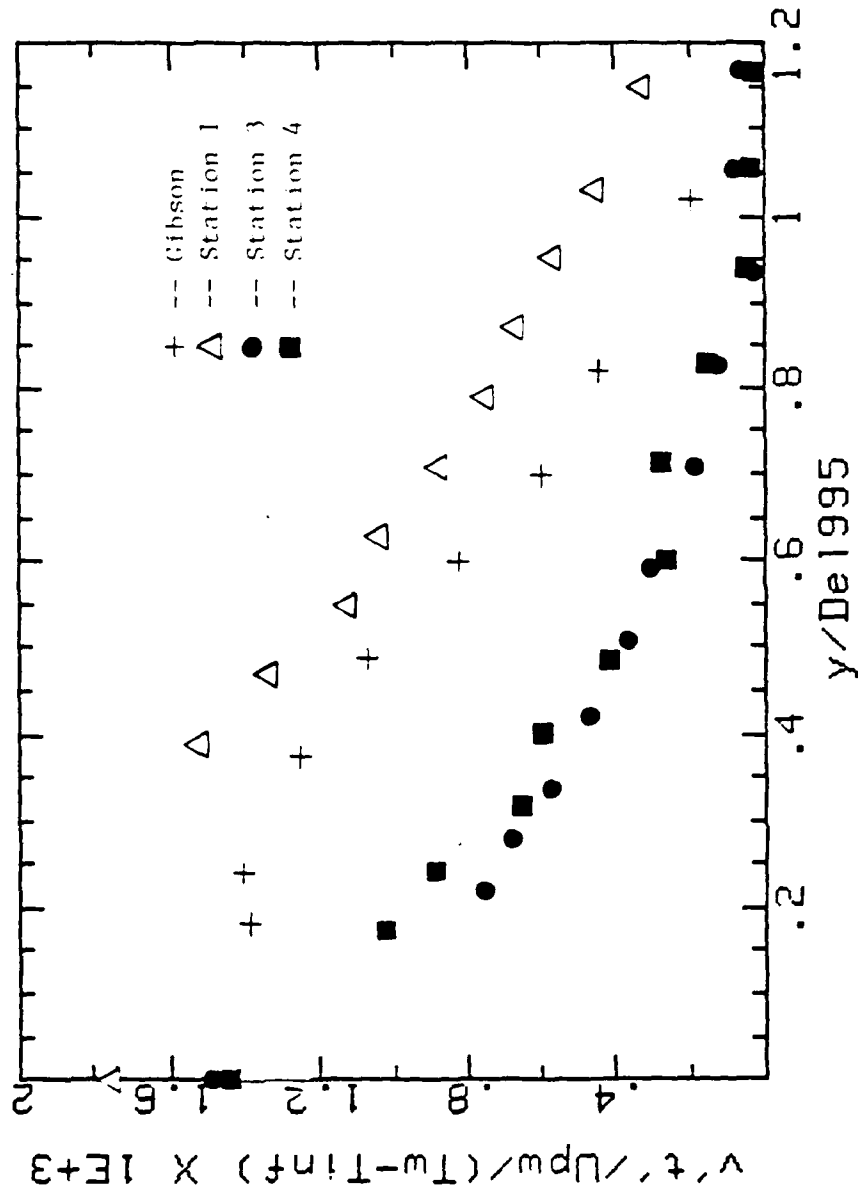


Figure 25. $v't'$ profiles ($TI = 2.0\%$)

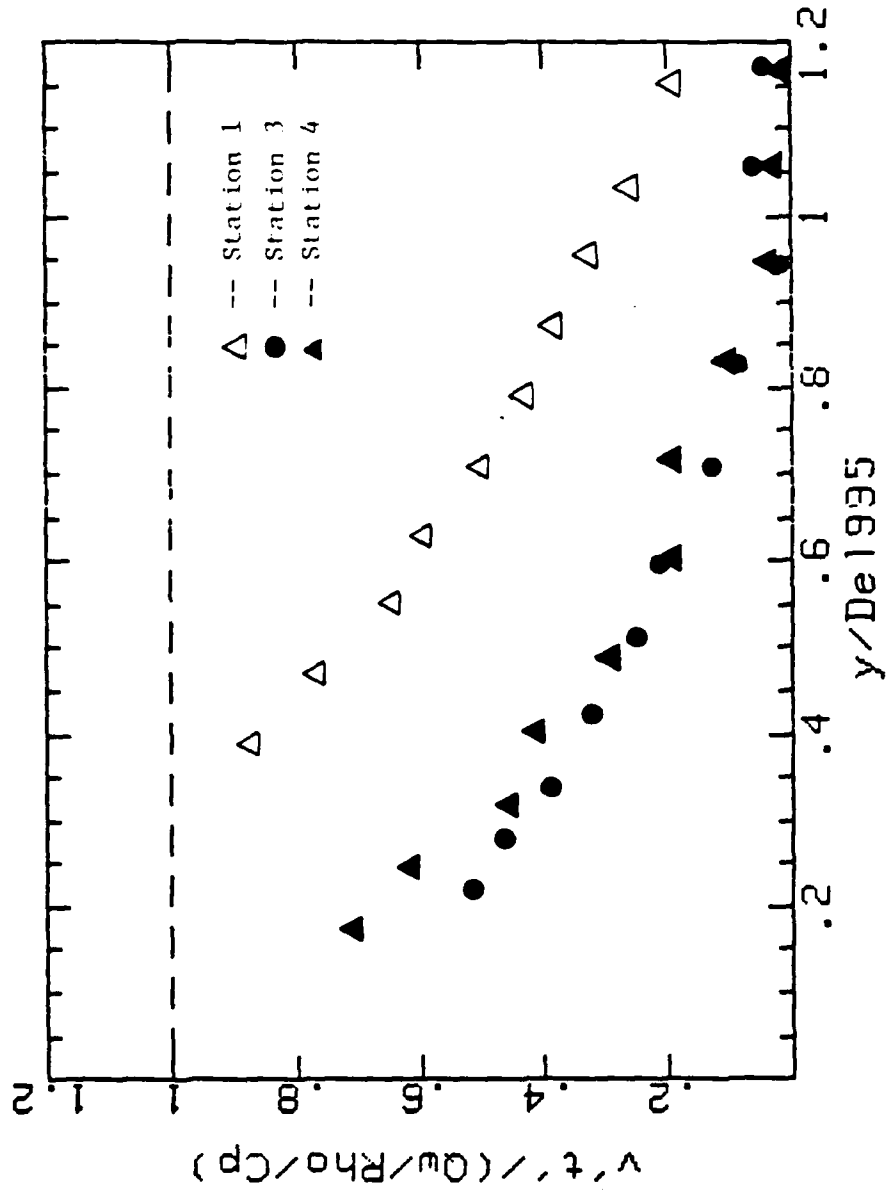


Figure 26. $v't'$ profiles normalized on wall heat flux ($TI = 2.0\%$)

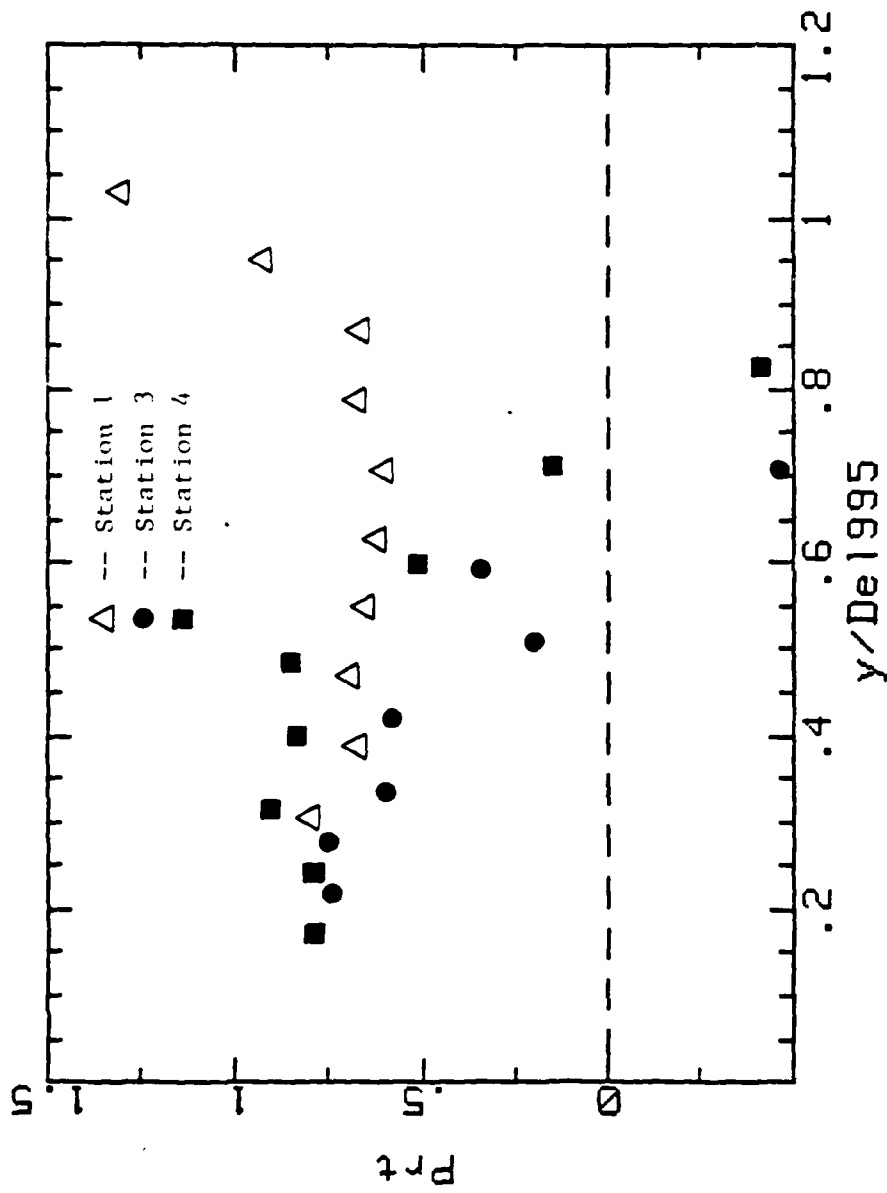


Figure 27. Turbulent Prandtl number profiles ($TI = 2.0\%$)

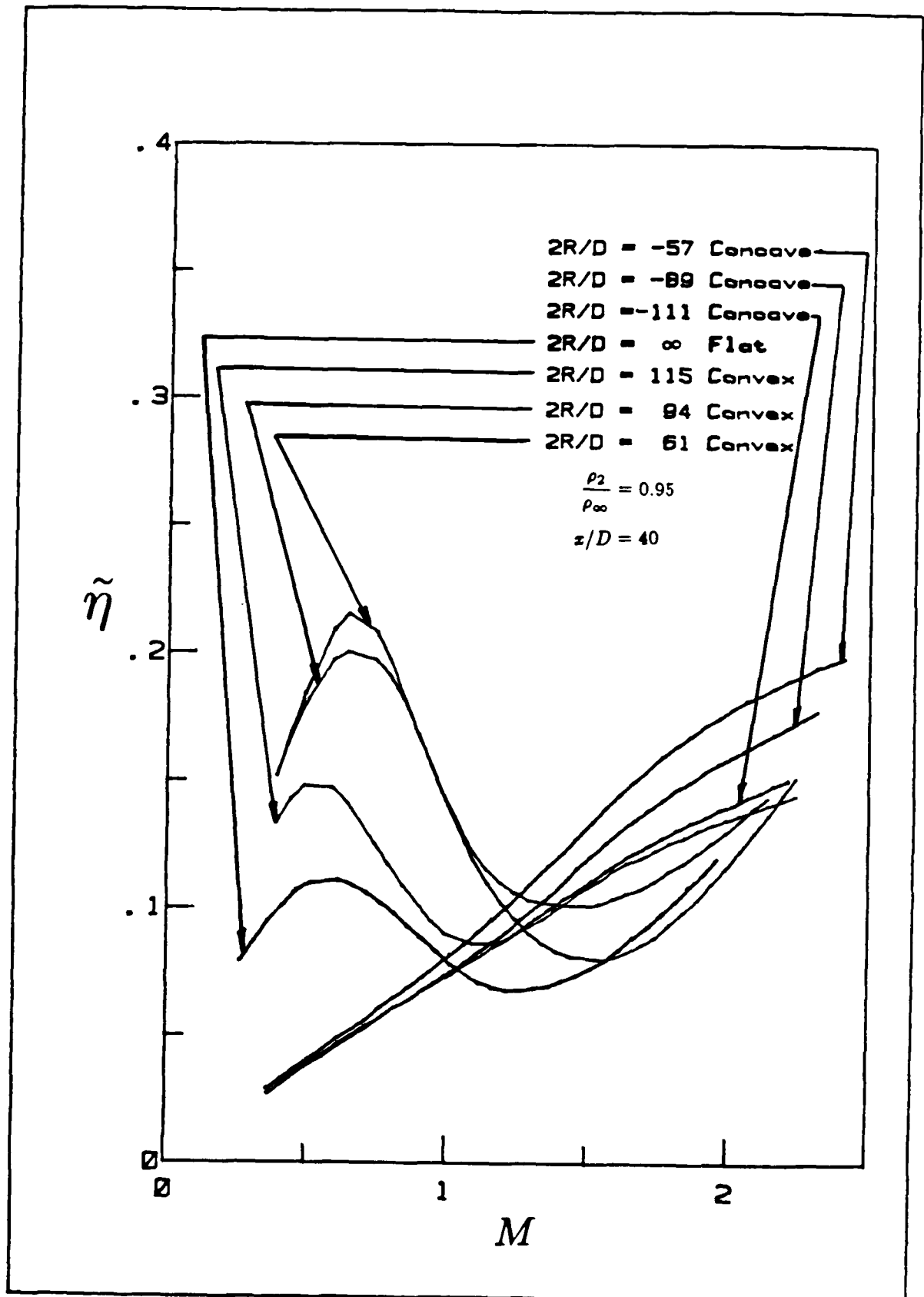


Figure 28. Film cooling on a curved surface

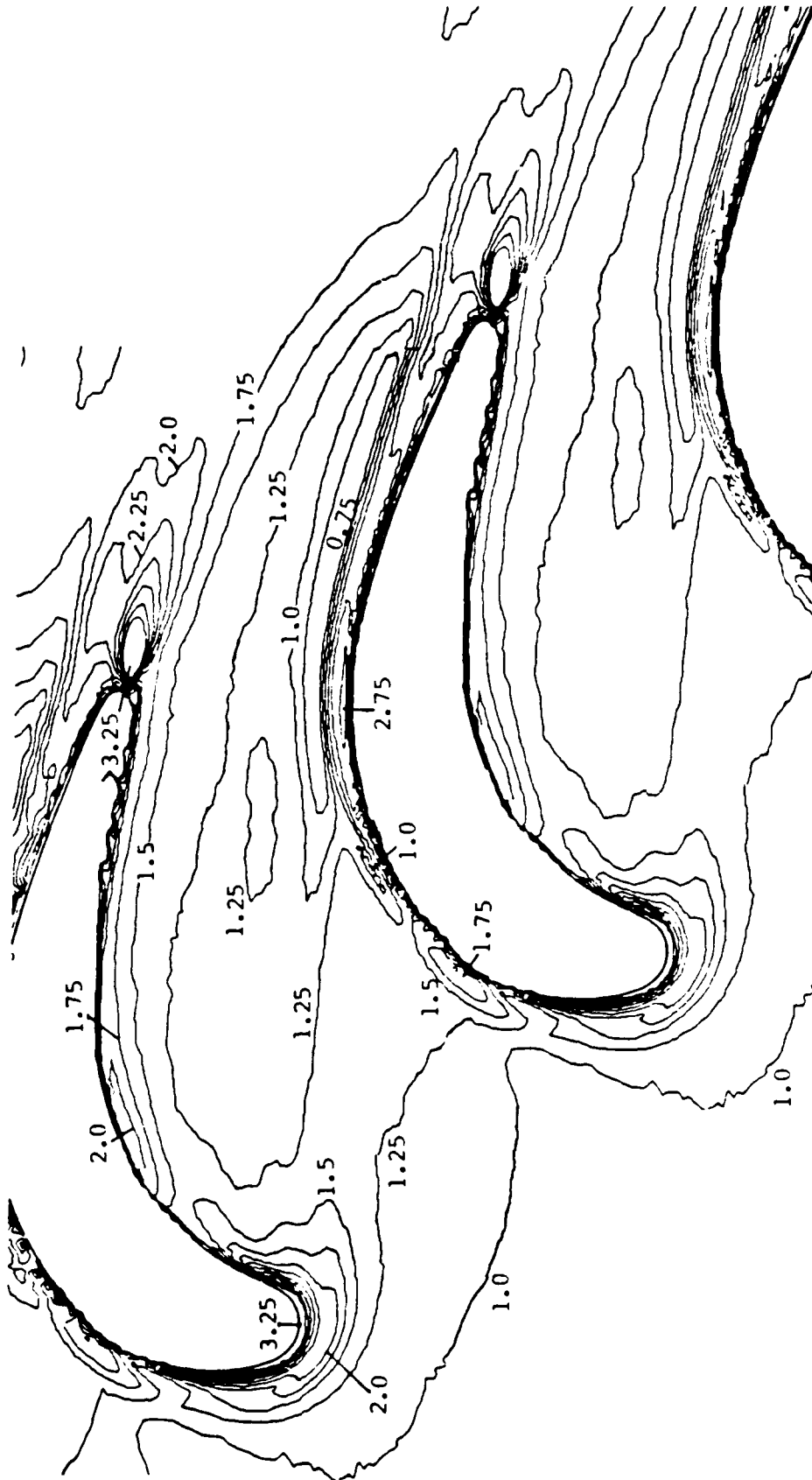


Figure 29. Case 2, thick boundary layer

Contours are of $St_m / St_{mo} =$

0.75, 1.0, 1.25, 1.5, 1.75, 2.0, 2.25, 2.5, 2.75, 3.0, 3.25

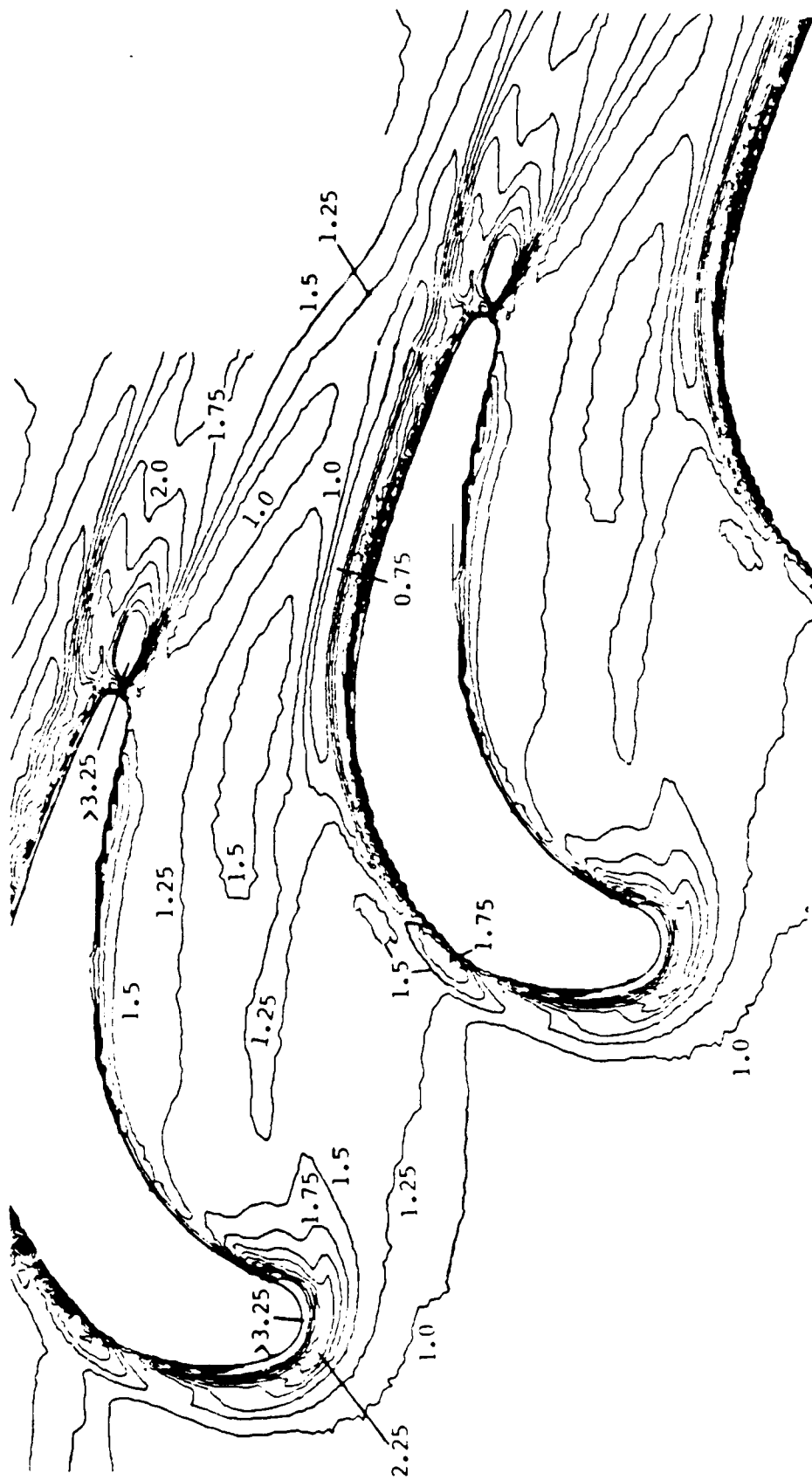


Figure 30. Case 3, low Reynolds number

Contours are of $St_m / St_{mo} =$

0.75, 1.0, 1.25, 1.5, 1.75, 2.0, 2.25, 2.5, 2.75, 3.0, 3.25

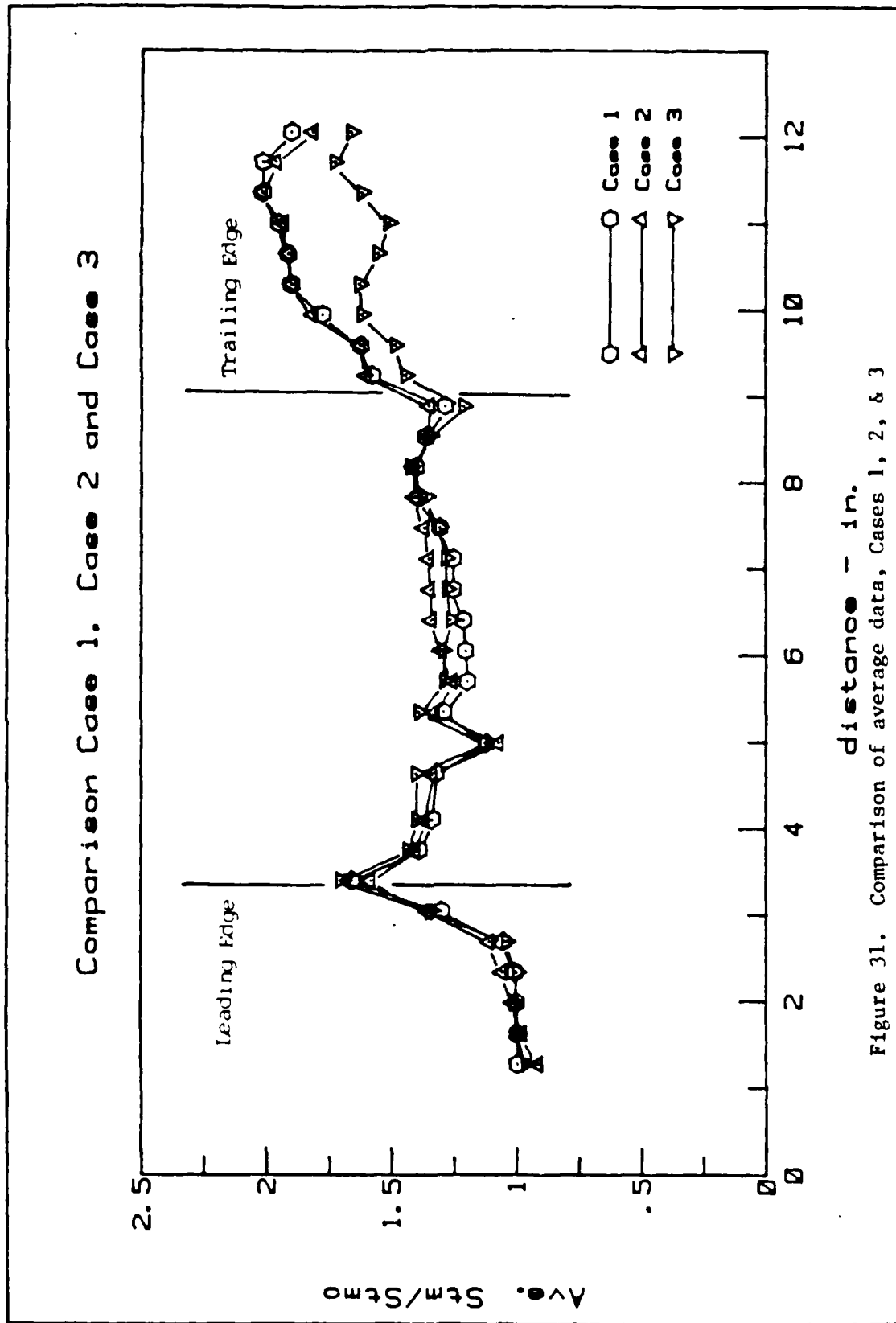


Figure 31. Comparison of average data, Cases 1, 2, & 3

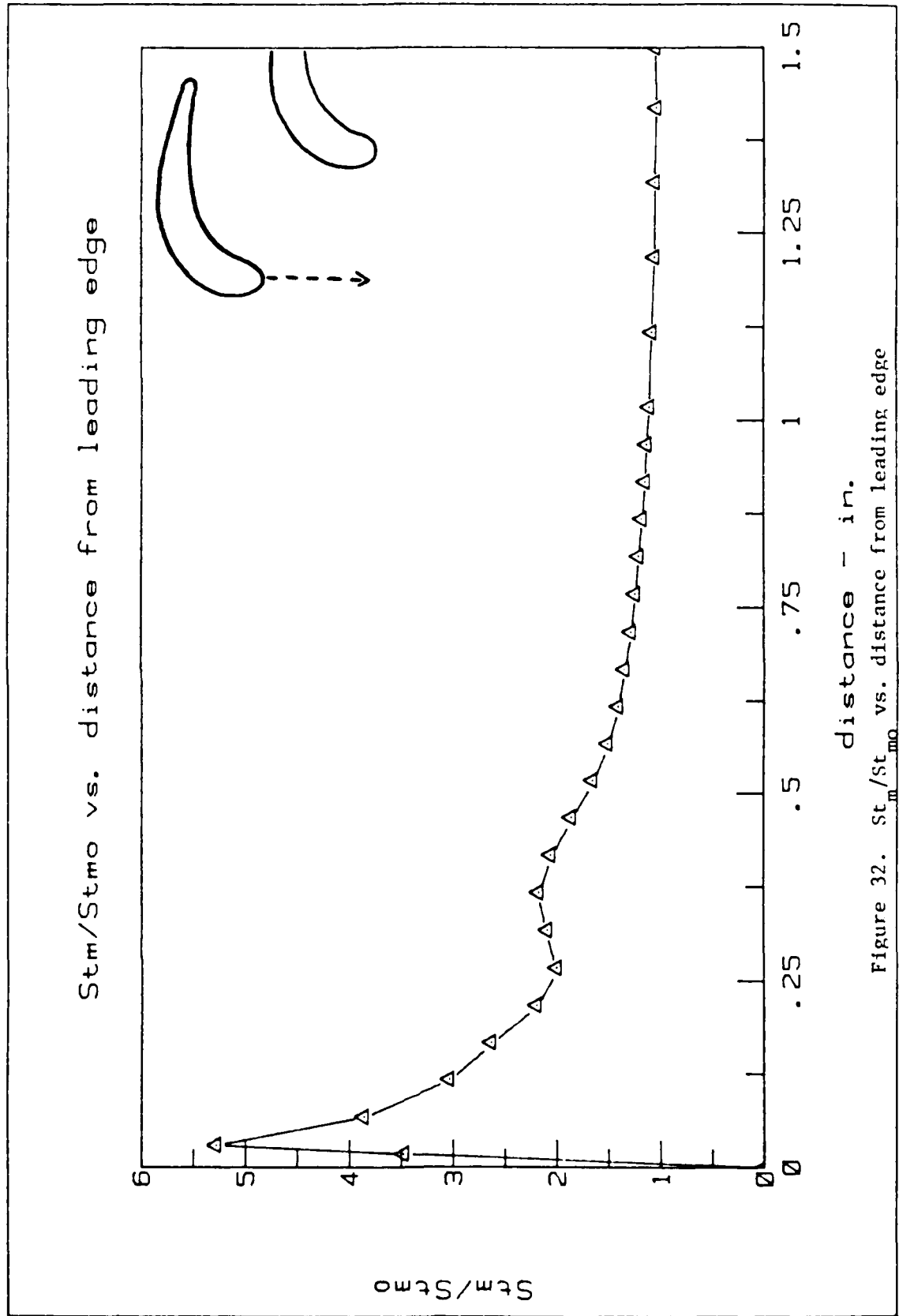
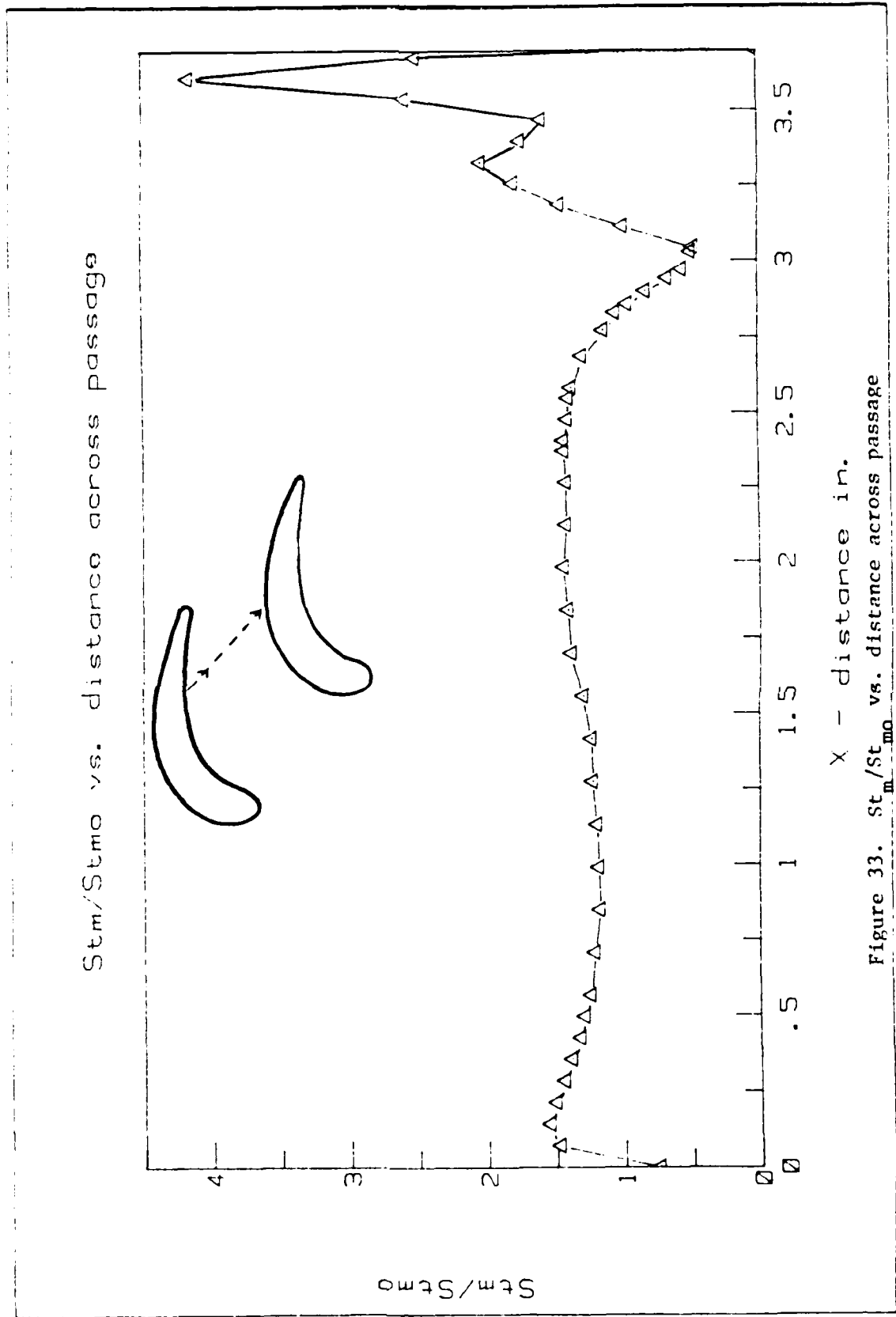


Figure 32. St_m/St_{mo} vs. distance from leading edge



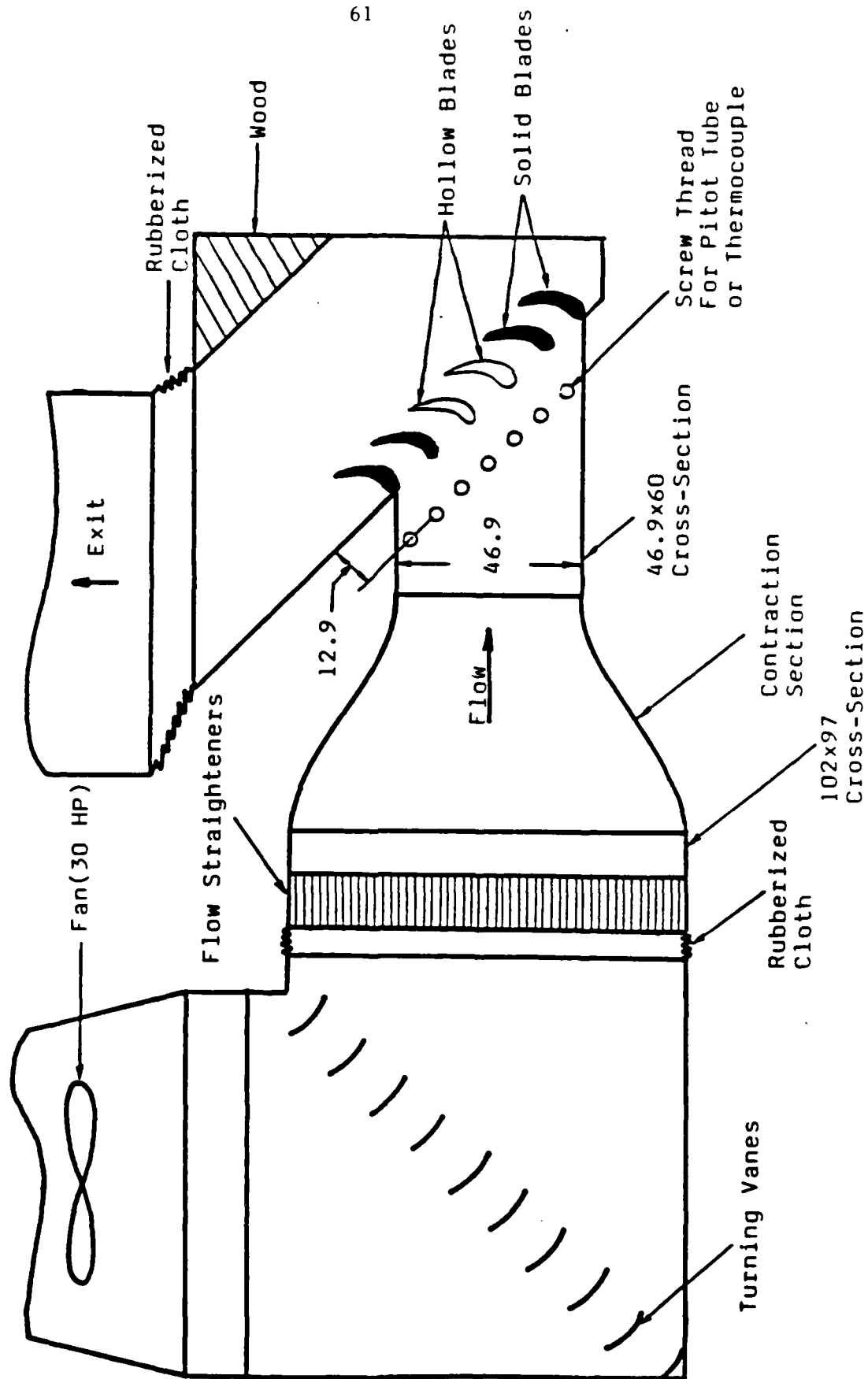


Figure 34. Schematic of wind tunnel and turbine cascade

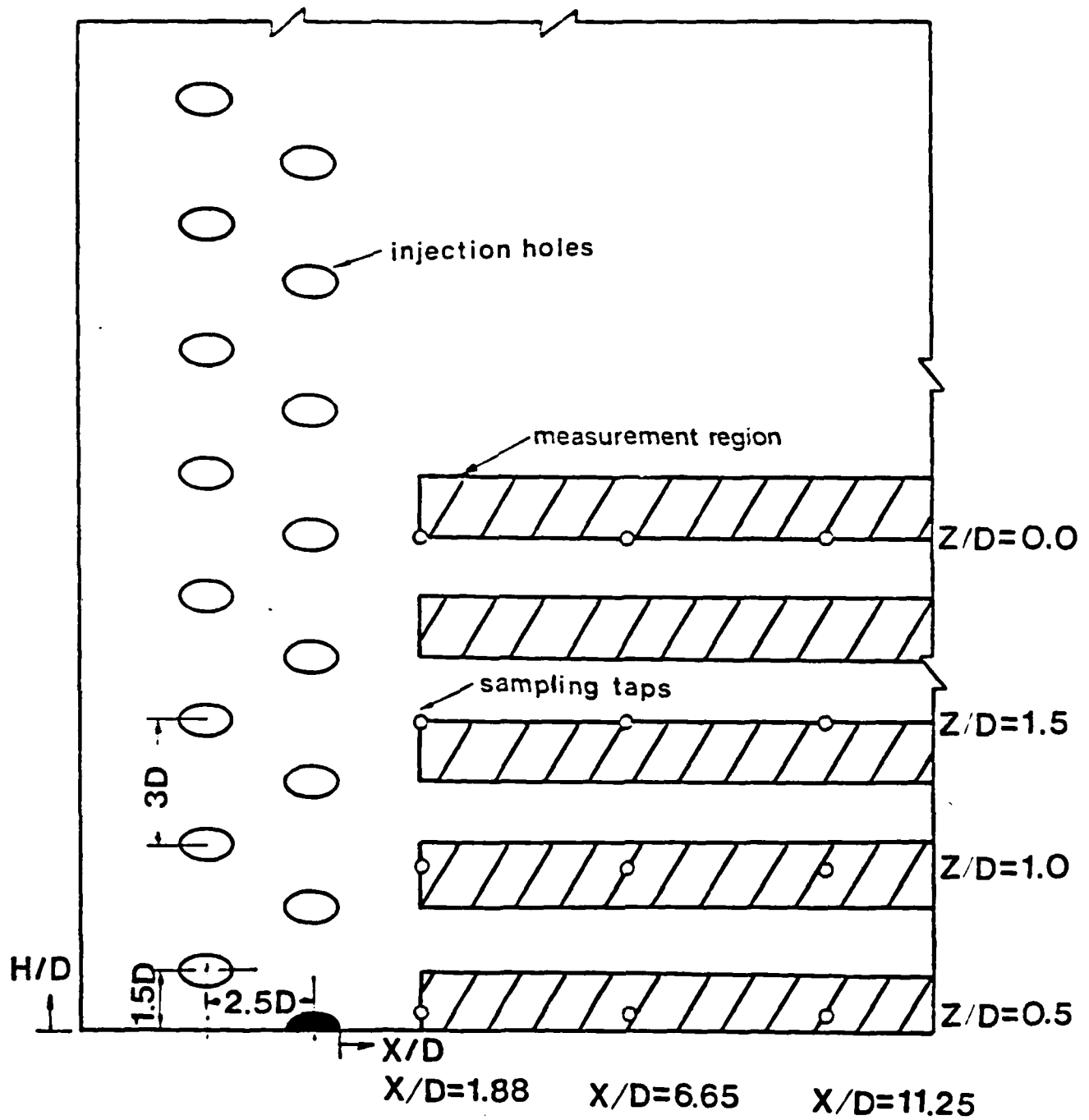
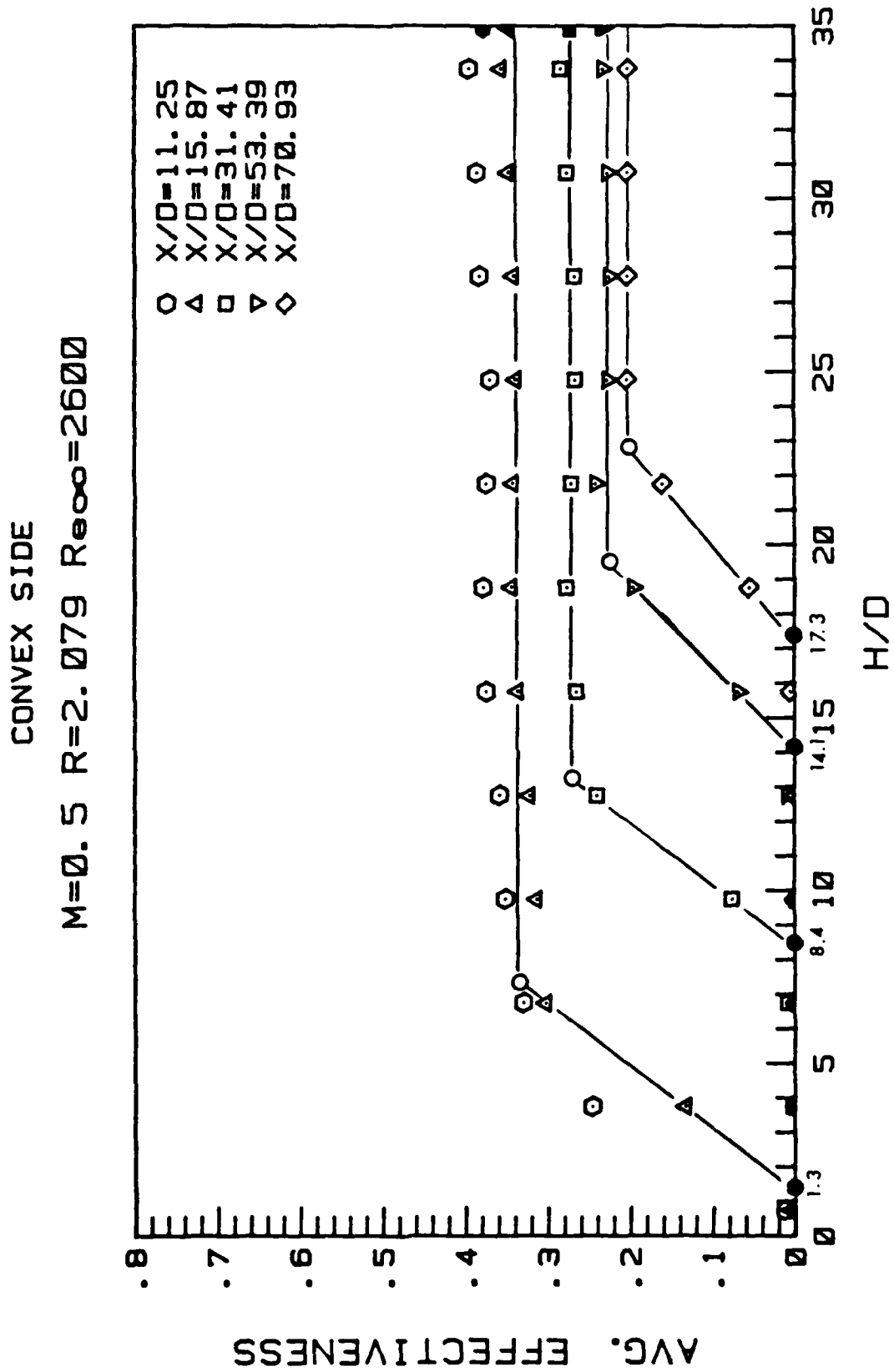


Figure 35. Detail of test blade showing measurement regions

Figure 36. Average film cooling effectiveness on convex surface at $M=0.5$

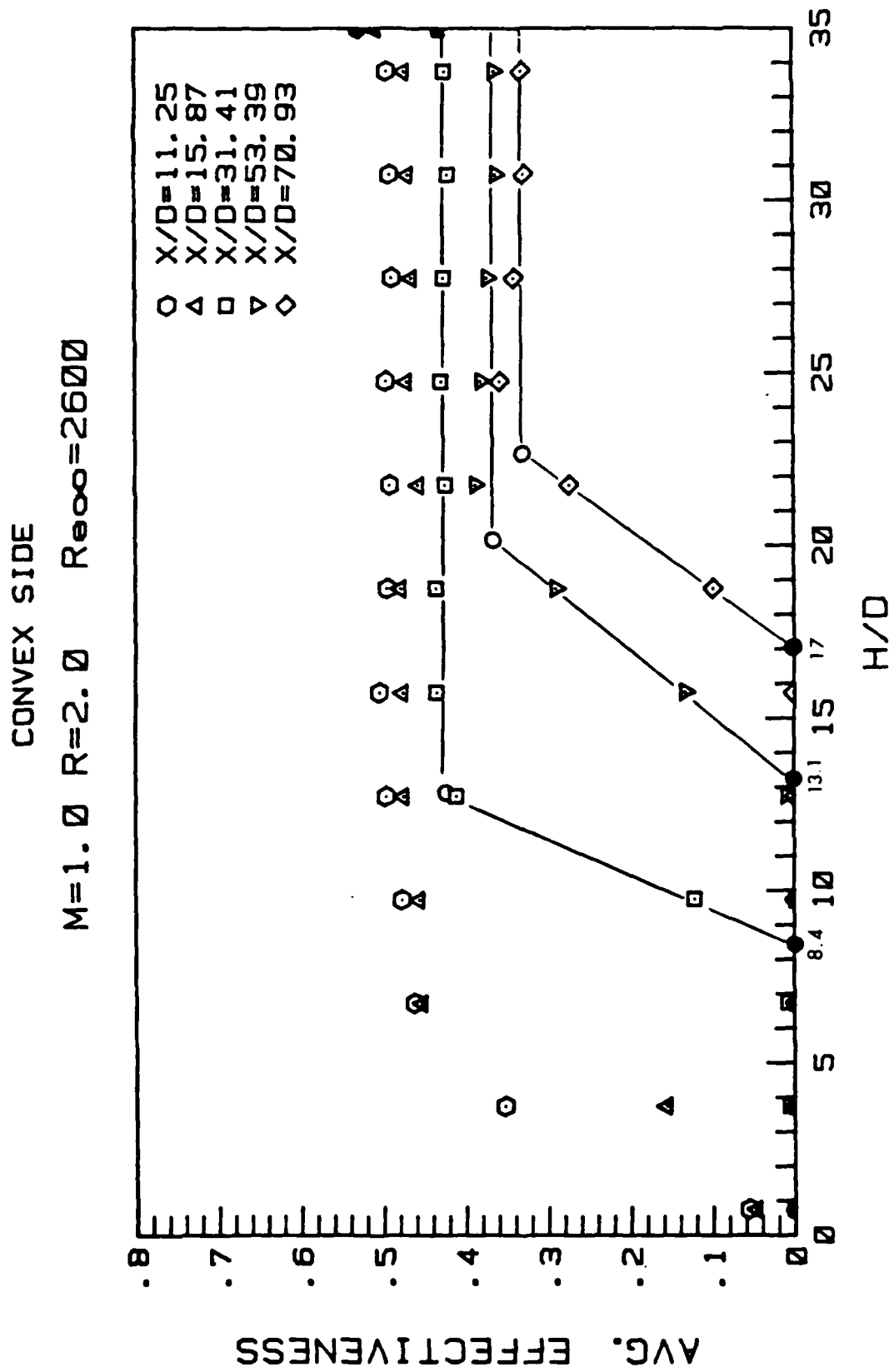
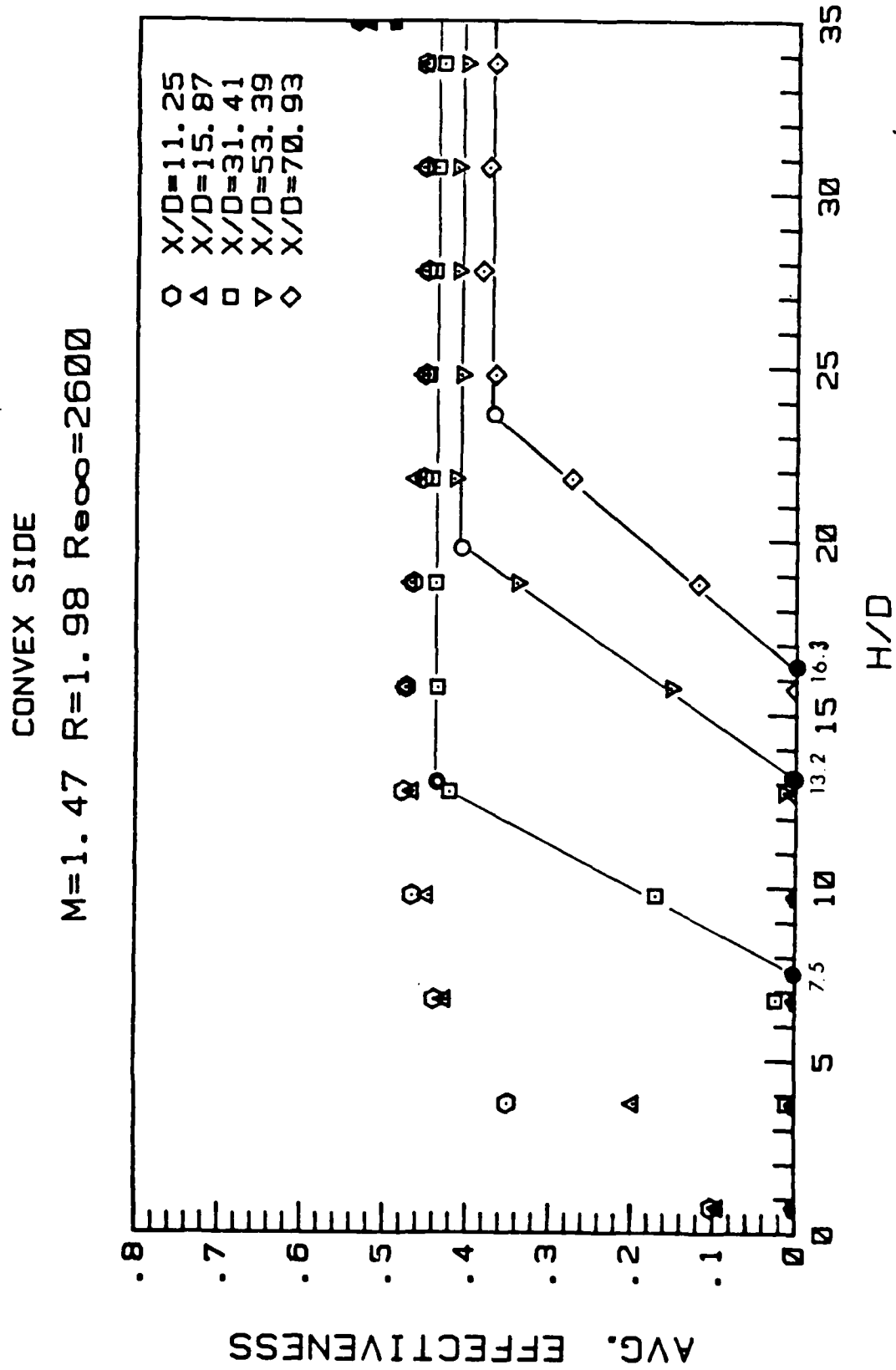


Figure 37. Average film cooling effectiveness on convex surface at $M=1.0$

Figure 38. Average film cooling effectiveness on convex surface at $M=1.47$

CONVEX SIDE
 $R=2.00 \quad Re_{\infty}=2600$

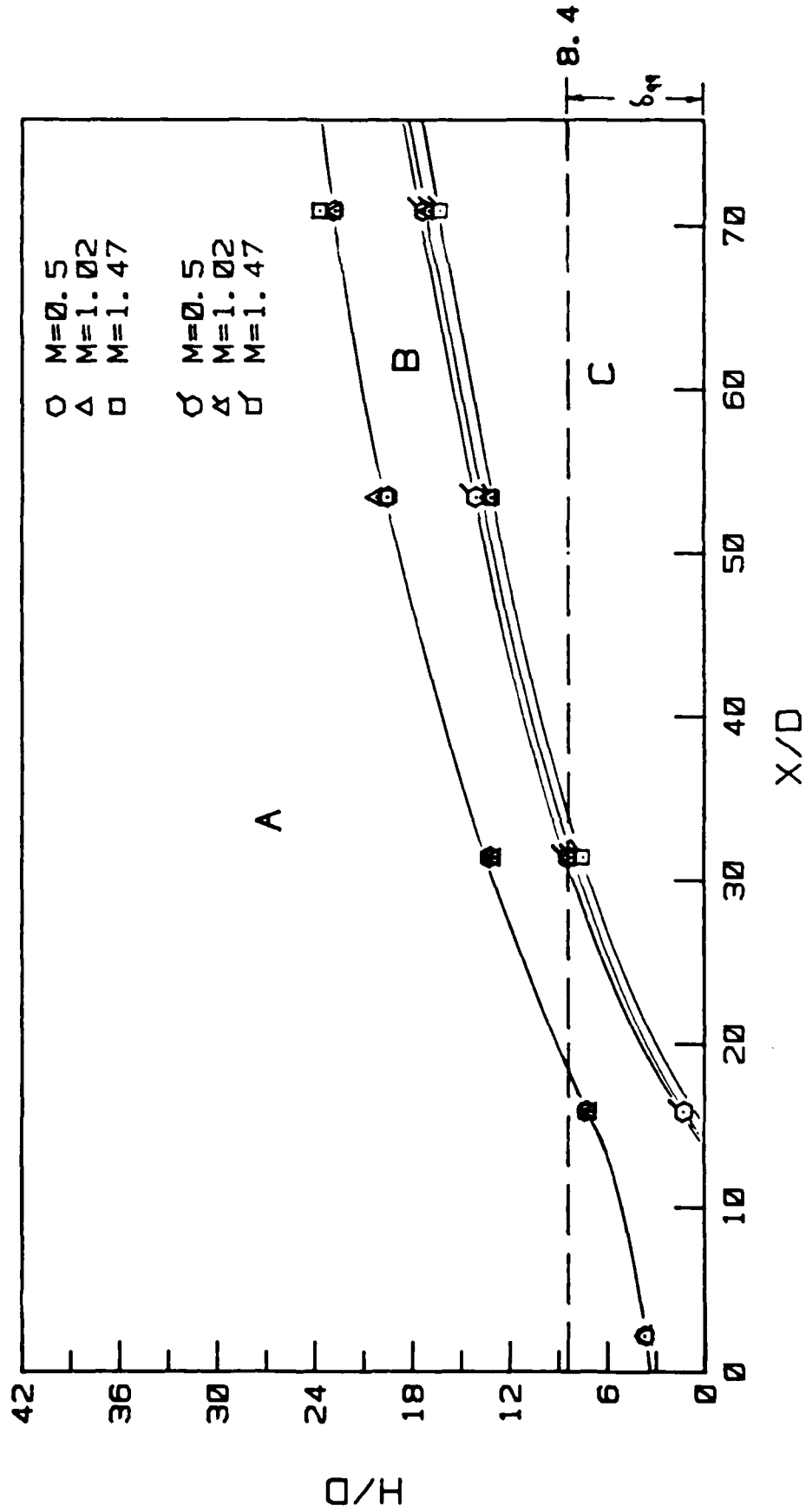


Figure 39. Distribution ranges of average film cooling effectiveness on the convex surface at near-end-wall region

CONVEX SIDE

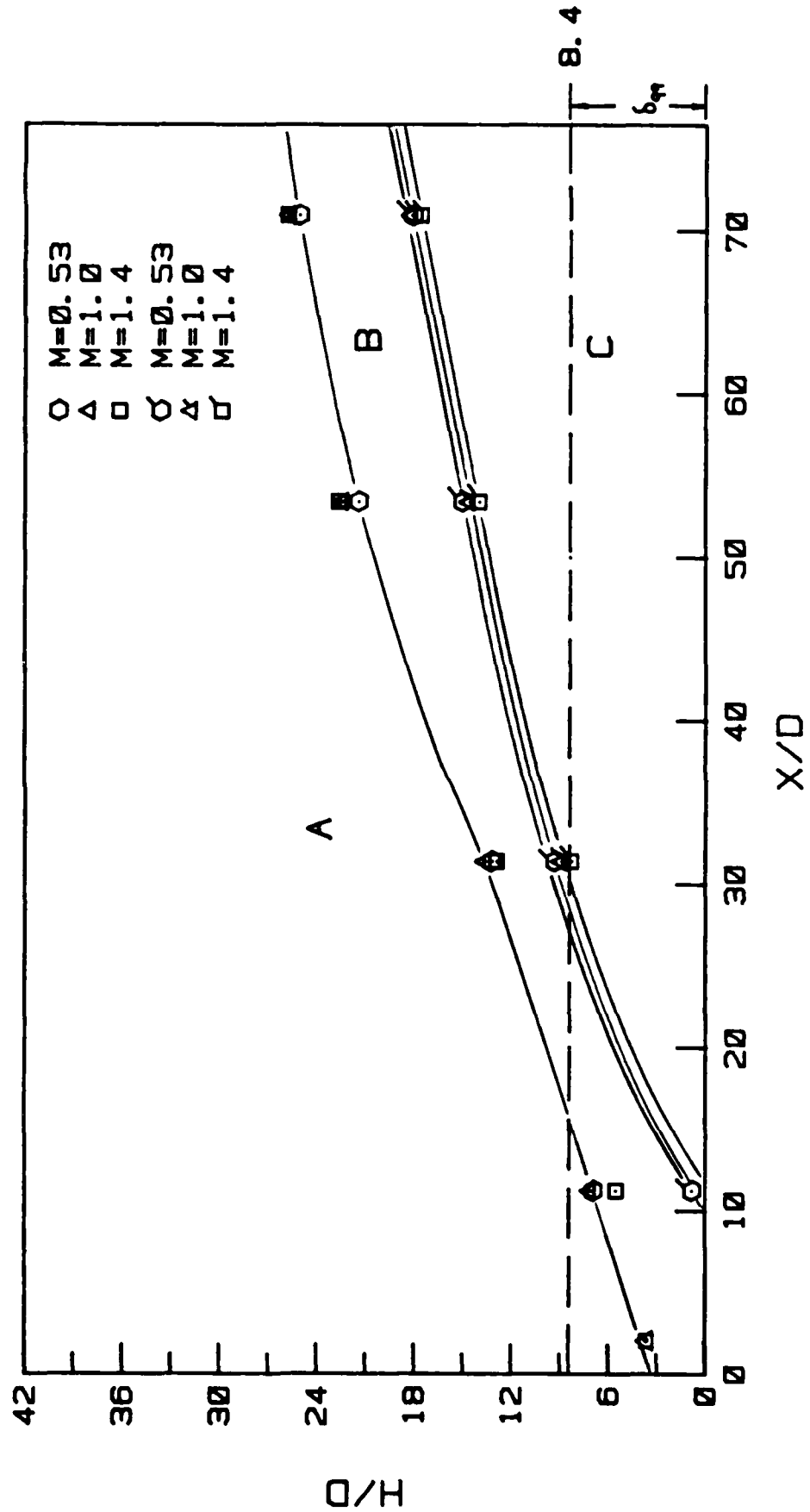
 $R=0.96 \quad Re_{\infty}=2600$ 

Figure 40. Distribution ranges of average film cooling effectiveness on the convex surface at near-end-wall region

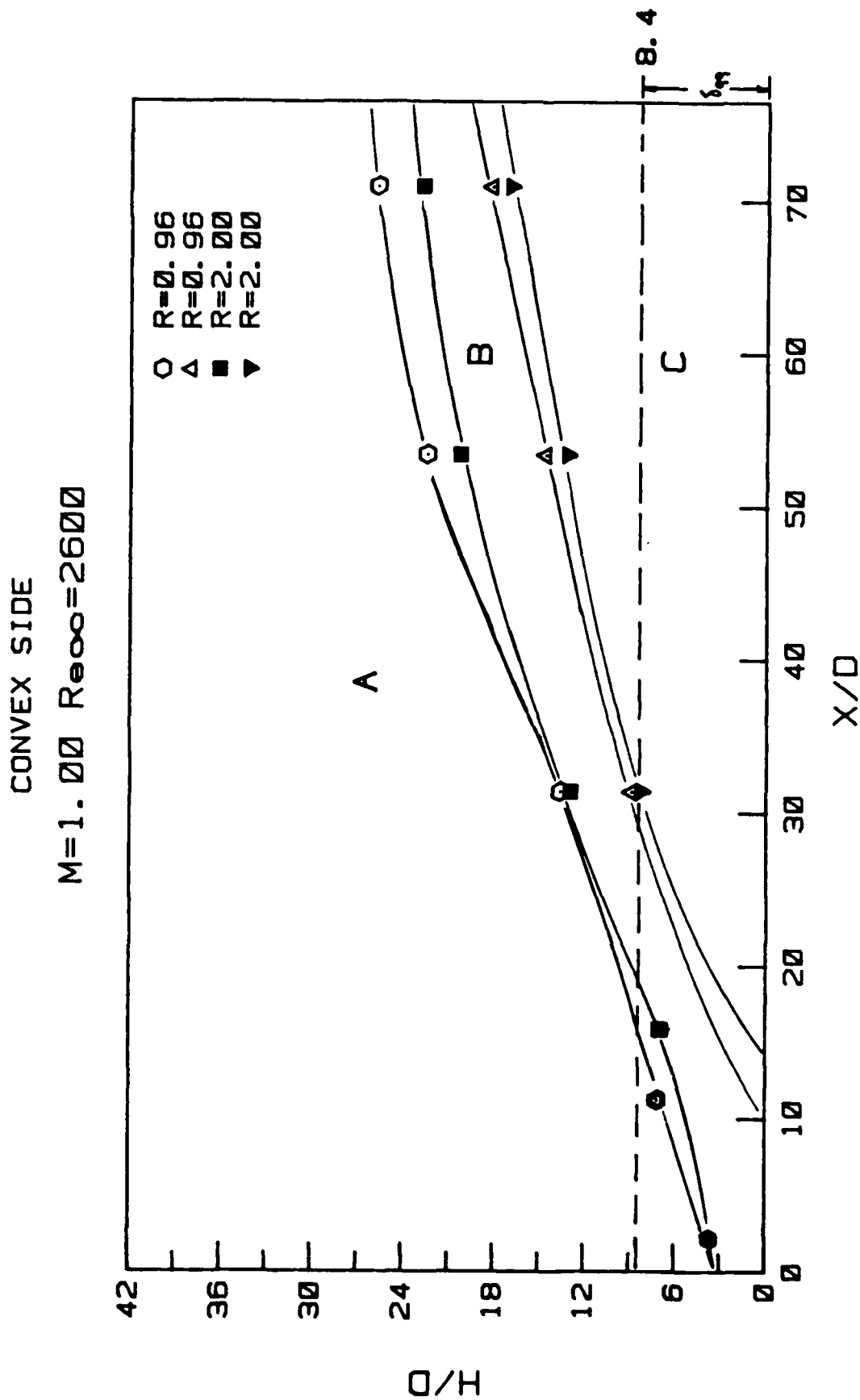


Figure 41. Comparison of distribution ranges of average film cooling effectiveness on the convex surface at near-end-wall region between two different density ratios

CONVEX SIDE

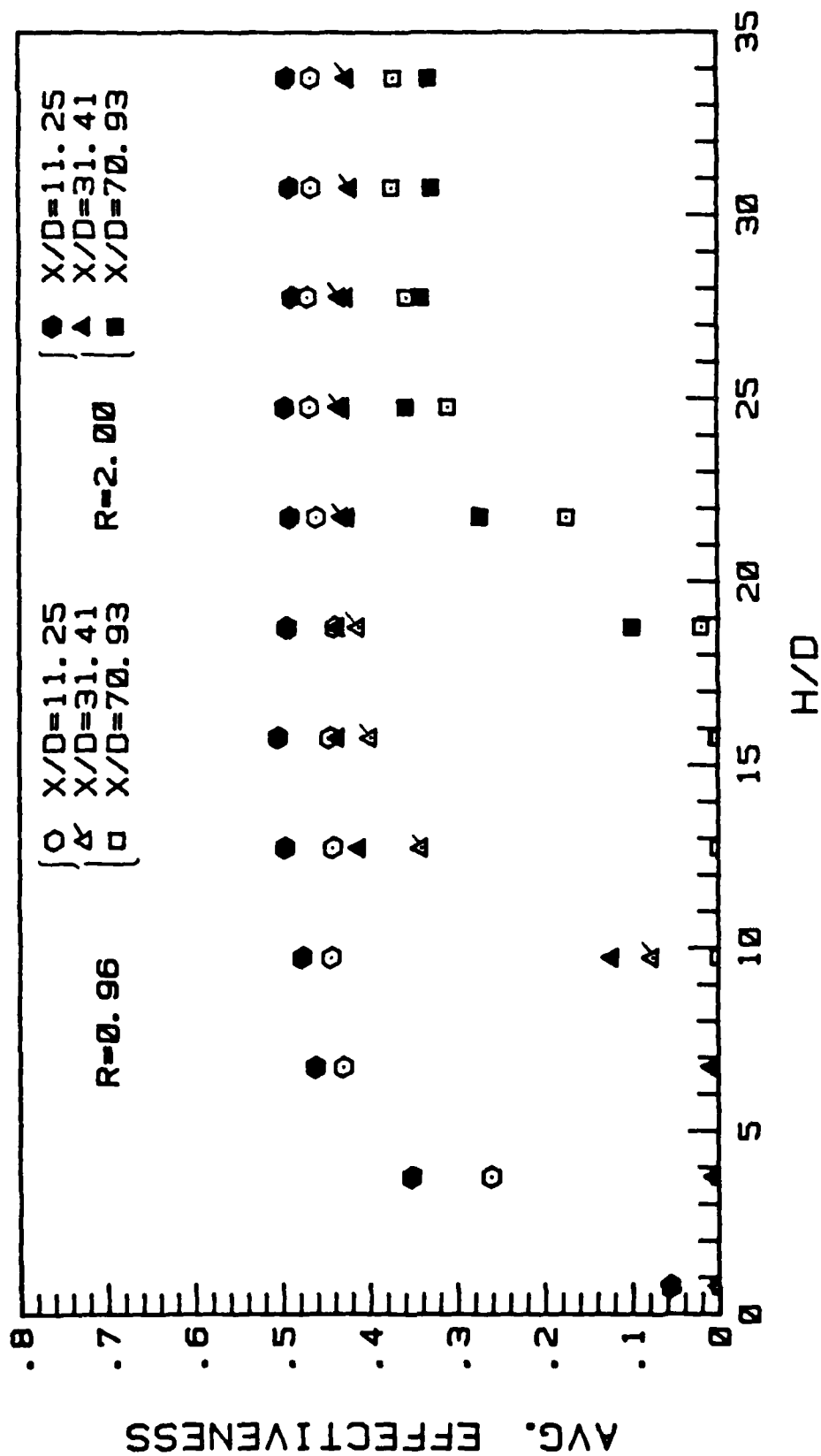
 $M=1.02$ $Re_{\infty}=2600$ 

Figure 42. Comparison of values of average film cooling effectiveness between two different density ratios

REFERENCES

- Abu-Ghannam, B. J. and Shaw, R., 1980, "Natural Transition of Boundary Layers--The Effects of Turbulence, Pressure Gradient, and Flow History," J. Mech. Engr. Sci., Vol. 22, No. 5, pp. 213-228.
- Adams, E. W. and Johnston, J. P., 1983, "A Mixing Length Model for Prediction of Convex Curvature Effects on Turbulent Boundary Layers," ASME Paper No. 83-GT-80.
- Barlow, R. S., Johnston, J. P., 1985, "Structure of Turbulent Boundary Layers on a Concave Surface," AFOSR Report MD 47.
- Blair, M. F. and Bennett, J. C., 1984, "Hot Wire Measurements of Velocity and Temperature Fluctuations in a Heated Turbulent Boundary Layer," 29th ASME International Gas Turbine Conference, Amsterdam.
- Bradshaw, P., 1973, "Effects of Streamline Curvature on Turbulent Flow," AGARD-AG-169.
- Champagne, F. H., Sleicher, C. A., and Wehrmann, O. H., 1967, "Turbulence Measurements with Inclined Hot-Wires, Parts 1 and 2," J. Fluid Mech., 28, pp. 153-182.
- Chen, K. K. and Thyson, N. A., 1971, "Extension of Emmon's Spot Theory to Flows on Blunt Bodies," AIAA J., Vol. 9, pp. 812-825.
- Crawford, M. E. and Kays, W. M., 1976, "STAN5--A Program for Numerical Computation of Two-Dimensional Internal and External Boundary Layer Flows," NASA CR-2742.
- Debruge, L. L., 1970, "A Theoretical Determination of Convection Heat-Transfer Coefficients During Transition on the Suction Side of Turbine Airfoils," AFAPL-TR-69-95.
- Dhawan, S. and Narasimha, R., 1985, "Some Properties of Boundary Layer Flow During Transition from Laminar to Turbulent Motion," J. Fluid Mech., Vol. 3, pp. 418-436.
- Dunham, K., 1972, "Predictions of Boundary Layer Transition on Turbomachinery Blades," AGARD-AG-164, pp. 55-71.
- Fulachier, L. and Dumas, R., 1976, "Spectral Analogy between Temperature and Velocity Fluctuations in a Turbulent Boundary Layer," J. Fluid Mech., 77, part 2, pp. 257-277.
- Gibson, M. M. and Verriopoulos, C. A., 1984, "Turbulent Boundary Layer on a Mildly Curved Convex Surface," Expt. in Fluids, 2, Springer-Verlag, pp. 73-80.

Gillis, J. C. and Johnston, J. P., 1983, "Turbulent Boundary Layer Flow and Structure on a Convex Wall and its Redevelopment on a Flat Wall," J. Fluid Mech., 135, pp. 123-153.

Hippensteele, S. A., Russell, L. M., Torres, F. J., 1985, "Local Heat-Transfer Measurements on a Large, Scale-Model Turbine Blade Airfoil Using a Composite of a Heater Element and Liquid Crystals," NASA Technical Memorandum 86900.

McCormack, P. P., Welke, H. and Kelleher, M., 1970, "Taylor Goertler Vortices and Their Effect on Heat Transfer," ASME Journal of Heat Transfer, Vol. 92, pp. 101-112.

Pedersen, D. R., 1972, "Effect of Density Ratio on Film Cooling Effectiveness for Injection through a Row of Holes and for a Porous Slot," Ph.D. Dissertation, University of Minnesota.

Sandborn, V. A., 1972, Resistance Temperature Transducers, Metrology Press, Fort Collins, CO, pp. 205-209.

Seyb, N. K., 1972, "The Role of Boundary Layers in Axial Flow Turbomachines and the Prediction of Their Effects," AGARD-AG-164, pp. 241-259.

Simmonich, J. C., Moffat, R. J., 1982, "Local Measurement of Turbulent Boundary Layer Heat Transfer on a Concave Surface Using Liquid Crystals," HMT, 35, Thermoscience Div., Mech. Eng. Dept., Stanford University.

Simon, T. W., Moffatt, R. J., Johnston, J. P., and Kays, W. M., 1980, "Turbulent Boundary Layer Heat Transfer Experiments: Convex Curvature Effects Including Introduction and Recovery," Rep. No. HMT-32, Thermosciences Div., Mech. Eng. Dept., Stanford University.

van Driest, E. R. and Blumer, C. B., 1963, "Boundary Layer Transition: Free-Stream Turbulence and Pressure Gradient Effects," AIAA J., Vol. 1, pp. 1303-1306.

Wang, T. and Simon, T. W., 1985, "Heat Transfer and Fluid Mechanics Measurements in Transitional Boundary Layers on Convex-Curved Surfaces," ASME Paper No. 85-HT-60.

Wang, T., Simon, T. W. and Buddhavarapu, J., 1985, "Heat Transfer and Fluid Mechanics Measurements in Transitional Boundary Layer Flows," ASME Paper No. 85-HT-113.

Wilson, D. J., 1970, "An Experimental Investigation of the Mean Velocity, Temperature, and Turbulence Fields in Plane and Curved Two-Dimensional Wall Jets: Coanda Effect," Ph.D. Thesis, U. of Minnesota.

Wyngaard, J. C., 1968, "Measurements of Small-Scale Turbulence Structure with Hot Wires," J. Phys. E. 1, pp. 1105-8.

You, S. M., 1986, "Turbulent Boundary Layer Heat Transfer and Fluid Mechanics Measurements on a Curved Convex Wall," M.S.M.E. Thesis, Dept. of Mech. Engrg., University of Minnesota.

You, S. M., T. W. Simon, and J. Kim, 1986a, "Boundary Layer Heat Transfer and Fluid Mechanics Measurements on a Mildly-Curved Convex Wall," Proc. Eighth Int. Heat Trans. Conf.

You, S. M., T. W. Simon, and J. Kim, 1986b, "Free-Stream Turbulence Effects on Convex-Curved Turbulent Boundary Layers," Submitted to the Gas Turbine Heat Transfer Session at the 1986 ASME Winter Annual Meeting.

END

10-86

DTIC